

IRC +10 216 in 3D: morphology of a TP-AGB star envelope[★]

M. Guélin^{1,2}, N. A. Patel³, M. Bremer¹, J. Cernicharo⁴, A. Castro-Carrizo¹, J. Pety¹, J. P. Fonfría⁴, M. Agúndez⁴,
M. Santander-García⁴, G. Quintana-Lacaci⁴, L. Velilla Prieto⁴, R. Blundell³, and P. Thaddeus³

¹ Institut de Radioastronomie Millimétrique, 300 rue de la Piscine, 38406 Saint Martin d'Hères, France
e-mail: guelin@iram.fr

² LERMA, Observatoire de Paris, PSL Research University, CNRS, UMR 8112, 75014 Paris, France

³ Center for Astrophysics, 60 Garden street, Cambridge, MA, USA

⁴ ICMM, CSIC, Group of Molecular Astrophysics, C/ Sor Juana Inés de la Cruz 3, Cantoblanco, 28049 Madrid, Spain

Received 21 July 2017 / Accepted 10 September 2017

ABSTRACT

During their late pulsating phase, AGB stars expel most of their mass in the form of massive dusty envelopes, an event that largely controls the composition of interstellar matter. The envelopes, however, are distant and opaque to visible and NIR radiation: their structure remains poorly known and the mass-loss process poorly understood. Millimeter-wave interferometry, which combines the advantages of longer wavelength, high angular resolution and very high spectral resolution is the optimal investigative tool for this purpose. Mm waves pass through dust with almost no attenuation. Their spectrum is rich in molecular lines and hosts the fundamental lines of the ubiquitous CO molecule, allowing a tomographic reconstruction of the envelope structure. The circumstellar envelope IRC +10 216 and its central star, the C-rich TP-AGB star closest to the Sun, are the best objects for such an investigation. Two years ago, we reported the first detailed study of the CO(2–1) line emission in that envelope, made with the IRAM 30-m telescope. It revealed a series of dense gas shells, expanding at a uniform radial velocity. The limited resolution of the telescope (HPBW 11'') did not allow us to resolve the shell structure. We now report much higher angular resolution observations of CO(2–1), CO(1–0), CN(2–1) and C₄H(24–23) made with the SMA, PdB and ALMA interferometers (with synthesized half-power beamwidths of 3'', 1'' and 0.3'', respectively). Although the envelope appears much more intricate at high resolution than with an 11'' beam, its prevailing structure remains a pattern of thin, nearly concentric shells. The average separation between the brightest CO shells is 16'' in the outer envelope, where it appears remarkably constant. Closer to the star (<40''), the shell pattern is denser and less regular, showing intermediary arcs. Outside the small ($r < 0.3''$) dust formation zone, the gas appears to expand radially at a constant velocity, 14.5 km s⁻¹, with small turbulent motions. Based on that property, we have reconstructed the 3D structure of the outer envelope and have derived the gas temperature and density radial profiles in the inner ($r < 25''$) envelope. The shell-intershell density contrast is found to be typically 3. The over-dense shells have spherical or slightly oblate shapes and typically extend over a few steradians, implying isotropic mass loss. The regular spacing of shells in the outer envelope supports the model of a binary star system with a period of 700 yr and a near face-on elliptical orbit. The companion fly-by triggers enhanced episodes of mass loss near periastron. The densification of the shell pattern observed in the central part of the envelope suggests a more complex scenario for the last few thousand years.

Key words. ISM: molecules – stars: AGB and post-AGB – astrochemistry – circumstellar matter – stars: individual: IRC +10 216 – stars: mass-loss

1. Introduction

Three-quarters of the matter returned to the interstellar medium (ISM) comes from AGB stars in their late thermally pulsating (TP) phase. The mass loss rate may then reach 10^{-5} to $10^{-4} M_{\odot} \text{ yr}^{-1}$ and the stars become enshrouded by a thick, dusty

[★] This work was based on observations carried out with the IRAM, SMA and ALMA telescopes. IRAM is supported by INSU/CNRS (France), MPG (Germany) and IGN (Spain). The Submillimeter Array is a joint project between the Smithsonian Astrophysical Observatory (USA) and the Academia Sinica Institute of Astronomy and Astrophysics (Taiwan) and is funded by the Smithsonian Institution and the Academia Sinica. This paper makes use of the ALMA data: ADS/JAO.ALMA#2013.1.01215.S & ADS/JAO.ALMA#2013.1.00432.S. ALMA is a partnership of ESO (representing its member states), NSF (USA) and NINS (Japan), together with NRC (Canada), NSC and ASIAA (Taiwan) and KASI (Republic of Korea), in cooperation with the Republic of Chile. The Joint ALMA Observatory is operated by ESO, AUI/NRAO and NAOJ.

envelope opaque to visible and near IR radiation. Given that the TP phase is short-lived, the closest AGB-TP stars are fairly distant. High visual opacity and distance conspire to make the mass loss mechanism and the envelope structure poorly understood, despite their importance for galactic evolution.

The advent of powerful millimeter/sub-mm interferometers that combine longer wavelengths with high angular and spectral resolution provides a unique opportunity to investigate these objects. Mm/sub-mm waves freely traverse the thickest dust layers, and the mm spectrum, rich in molecular lines, yields detailed information on the gas physical conditions, its chemical content and, mostly, on the velocity field. The latter often reduces to uniform radial expansion, allowing the 3-dimensional envelope structure to be recovered. We present in this paper the first high resolution study of the entire IRC +10 216 envelope, the archetype of TP-AGB star envelopes, carried out in the $J = 2-1$ line of CO, the best single tracer of the molecular gas in this type of object (Ramstedt et al. 2008).

The envelope IRC +10 216¹ (CW Leonis), which surrounds the closest C-rich TP-AGB star to the Sun (hereafter denoted CW Leo★), is of particular interest. Located at a distance of ~ 130 pc (Menten et al. 2012), it appears on optical images as a dark spherical cloud that extends over several arcmin. Some 80 molecular species, half of all known interstellar molecules, have been detected in this envelope through thousands of millimeter-wave lines (Cernicharo et al. 2000). Remarkably, all line profiles but those arising from the tiny dust-acceleration region have the same width in the direction of the star: 29 km s^{-1} . Since the molecular lines arise at different distances from the central star – e.g. SiO and SiS are restricted to the central region, whereas the CO is distributed over the whole envelope – the constant line width implies a steady expansion velocity along the line of sight, 14.5 km s^{-1} , and a small turbulent velocity. The systemic velocity of the envelope is -26.5 km s^{-1} relative to the local standard of rest (LSR).

IRC +10 216 has been the object of numerous studies in so far as dust and molecular content are concerned. Of particular relevance to this work are *a*) the CFHT, *Hubble* and VLT V-light images of the scattered IS light (Mauron & Huggins 2000, 2006; Leão et al. 2006), which revealed the presence of a ringed dust structure (Fig. 13); *b*) the detection of UV emission from a termination shock (or *astrosphere*) that marks the impact of the outflowing gas on the surrounding ISM at $15'$ (≈ 2 pc) NE of CW Leo★ (Sahai & Chronopoulos 2010); and *c*) the FIR emission map made with the PACS instrument on *Herschel* (Decin et al. 2011). The $100 \mu\text{m}$ map, like the visible light images, shows a succession of rings that mark the rims of dense spherical shells. Finally; *d*) interferometric images of the mm line emission of a score of reactive molecules, such as CN, CCH and HC_5N , show that these species are mostly confined inside a thin spherical shell of radius $15''$ whose center, curiously, is offset by $2''$ from CW Leo★ (Guélin et al. 1993a).

We have previously reported a detailed study of IRC +10 216 made in the $^{12}\text{CO}(2-1)$ and $^{12}\text{CO}(1-0)$ lines (hereafter denoted CO(2–1) and CO(1–0)) and in the $^{13}\text{CO}(1-0)$ line with the IRAM 30-m telescope (Cernicharo et al. 2015). The CO(2–1) line emission was mapped throughout the entire envelope at a resolution of $11''$ (HPBW) and the line was continuously detected up to the photodissociation radius $r_{\text{phot}} \approx 180''$, inside which CO efficiently self-shields from interstellar UV radiation. The CO envelope fits well inside the large bow-shock traced by the UV emission, which suggests it expands freely inside the cavity cleared up by the shock (both the ^{12}CO and the ^{13}CO line profiles have the canonical full width of 29 km s^{-1}). It consists of a bright central peak, a broad, slowly decreasing pedestal and, superimposed on the pedestal, a series of over-dense gas shells.

The limited angular resolution of the 30-m telescope did not allow us to resolve the shell structure. So, we turned to the SMA, PdB and ALMA interferometers for much higher resolution observations. The envelope was fully mapped in CO(2–1) with the SMA at $3''$ resolution, and partly with PdBI at $1''$ resolution. The central 1-arcmin region was mapped in the CO(1–0), $^{13}\text{CO}(1-0)$, CN(2–1) and $\text{C}_4\text{H}(24-23)$ lines with the ALMA 12-m antennas and, for the short spacings, with the IRAM 30 m-diameter single-dish (SD) telescope. In Sect. 2, we describe the observations and data reduction procedures, and in Sects. 3 and 4 derive the envelope morphology, velocity field and gas physical

¹ Designation from the two-micron sky survey (Neugebauer & Leighton 1969), composed of the survey declination strip and a serial number. The name IRC +10216, was condensed into IRC +10216 by Becklin et al. (1969).

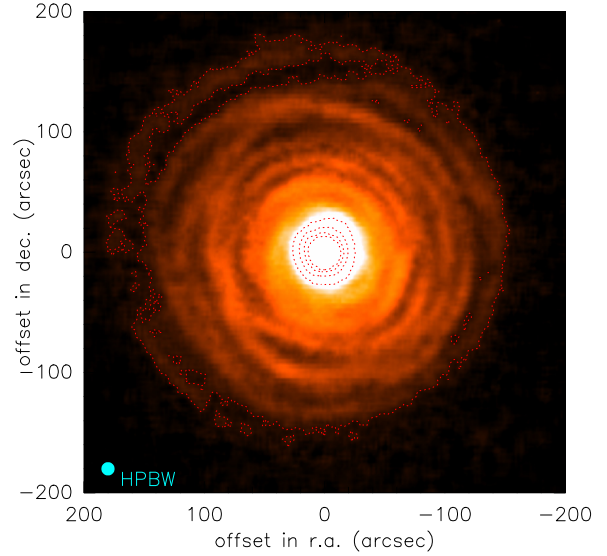


Fig. 1. Main beam-averaged $^{12}\text{CO}(2-1)$ line brightness temperature observed in IRC +10 216 with the IRAM 30-m telescope (HPBW $11''$) at the star velocity ($V_* = -26.5 \text{ km s}^{-1}$, $\Delta v = 2 \text{ km s}^{-1}$; see Cernicharo et al. (2015)). Dotted contours range from 1 to 50 K. On this, as on the other velocity-channel maps, the brightness scale is linear.

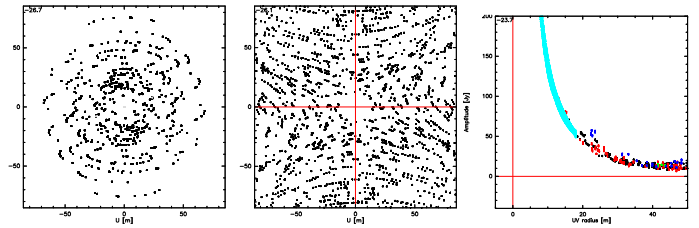


Fig. 2. Observed visibilities in the central 100 m of the UV-plane for the SMA (*left*) and ALMA (*middle*) observations. Thanks to the subcompact configuration, the shortest spacings for the SMA are as small as 6-m. *Right*: visibility amplitudes versus radius for the merged ALMA+single dish observations. The 30-m telescope amplitudes (blue dots) have been scaled by a factor of 0.8 to match the ALMA ones (red dots) in the overlap region.

properties. Finally, in Sect. 5, we interpret the results in terms of mass-loss by a binary star system.

2. Observations and data reduction

2.1. SMA observations

The SMA observations were made between Dec. 2011 and May 2013 in the Compact configuration and in May 2013 in the Subcompact configuration. Depending on the observing period, the array consisted of 7 or 8×6 -m diameter antennas. The antenna HPBW at the frequency of the CO(2–1) line (230.53797 GHz) is $54.6''$. The observations were made during Winter and Spring, mostly during night time. The precipitable water vapor was < 4 mm and the sky zenith opacity at 220 GHz between 0.1 and 0.3. The receivers were tuned so that the CO($J = 2-1$) line was in the LSB, centred on unit s16 of the 4 GHz bandwidth ASIC spectral correlator. The spacing between adjacent frequency channels was originally 812 kHz, but the data in Fig. 3 were binned to 1625 kHz (2.1 km s^{-1} at the CO(2–1) line frequency) to reduce the channel noise and suppress the overlap between adjacent channels.

We used the mosaic mode through a series of observing loops of typically 50 pointings, spaced by $25''$ (0.45 HPBW) in RA and

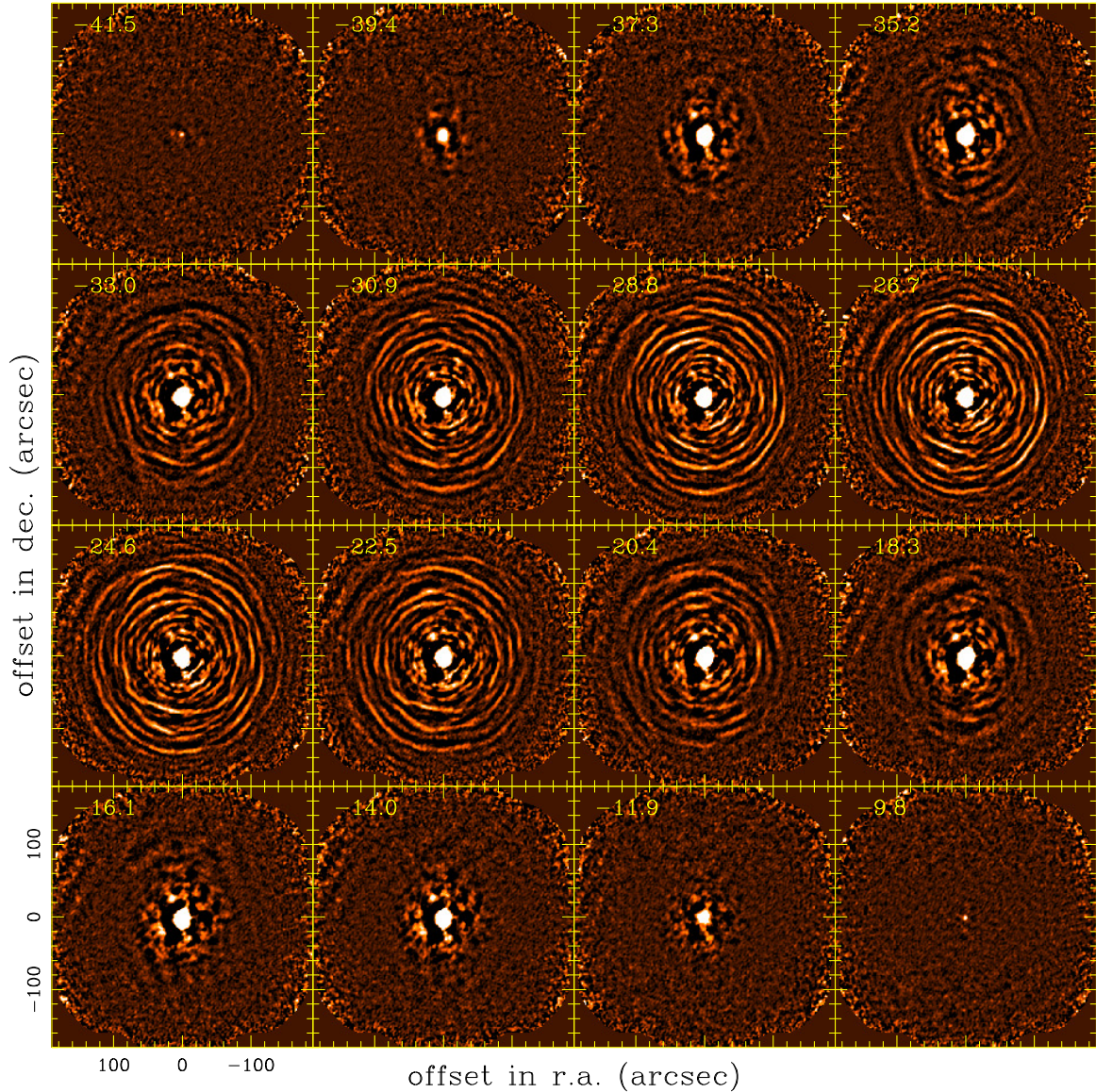


Fig. 3. Velocity-channel maps of the CO(2–1) line emission in the central $400'' \times 400''$ area of the IRC +10 216 envelope, observed with the SMA at a spatial resolution of $3.7'' \times 3.0''$ (HPBW, PA = -51°). The spectra have been binned to a resolution of 2.1 km s^{-1} ; velocities are relative to the LSR; the star systemic velocity is $V_* = -26.5 \text{ km s}^{-1}$; velocities more positive or more negative correspond to the rear and front parts of the envelope, respectively. The lack of visibilities $< 6 \text{ m}$ carves a negative bowl and black areas at the center of the maps (see text).

Dec. Two such loops were observed during a typical 10 h track. A total of 157 pointings were observed covering a nearly circular area of diameter $\approx 400''$. The signal phase and amplitude were calibrated by observing the quasars 0854+2006 and 0927+390 every 20 min. The antenna pointing was checked prior to each observing loop and the flux scale calibrated by observing Titan and/or Callisto on every track, as is standard in SMA observations. The receiver bandpass was also calibrated by observing 3C279 on every track.

The SMA data were calibrated using the MIRIAD calibration package (Sault et al. 1995). Calibrated *uvfits* files were converted into GILDAS format and further data processing and analysis was made with the GILDAS/MAPPING/MOSAIC data reduction software². The continuum signal was derived for each pointing by averaging the line emission-free channels of the 4 GHz-wide correlator and was subtracted from the original data to yield the CO(2–1) line data. The latter were first processed

alone to produce a first position-velocity datacube, then reprocessed after completing the SMA visibilities with short spacing pseudo-visibilities from the 30-m SD telescope, to produce a second position-velocity datacube. The steps in the second reduction were: (a) processing the SD data to derive pseudo-visibilities compatible with the SMA visibilities of each mosaic field; (b) checking the relative calibration of both instruments; (c) adding for each field the single-dish pseudo-visibilities with spatial frequencies between 0 and 20 m to the SMA visibilities; (d) Fourier transform the so-merged visibilities to derive the CO(2–1) *dirty* map of each field; (e) correct these maps for primary beam attenuation after truncating them at the 20% attenuation level and combine them into a single *dirty* image; finally (f) deconvolve the *dirty* map by the *dirty* beam to produce the final clean images, using a modified Hogböm algorithm that proceeds iteratively by order of decreasing signal-to-noise ratio.

The whole (a) to (f) procedure is as described in the GILDAS MAPPING Documentation. Step (b) was made by comparing the amplitudes of the azimuthally averaged pseudo-visibilities

² <http://www.iram.fr/IRAMFR/GILDAS>

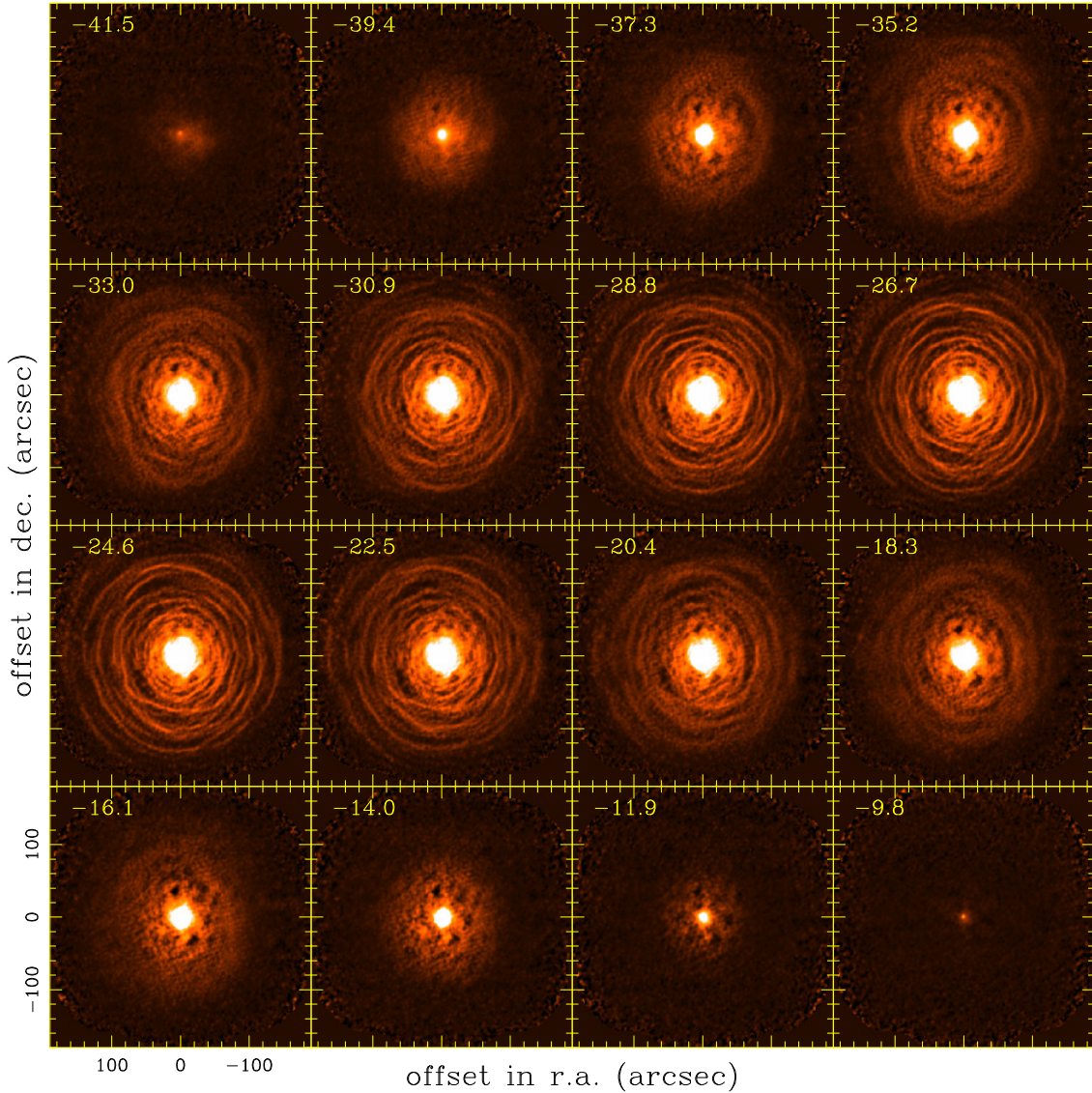


Fig. 4. Velocity-channel maps of the CO(2–1) line emission after combining the SMA data and the 30-m SD telescope data (see text). The spatial resolution is $3.8'' \times 3.1''$ (HPBW, PA = -51°). The spectra have been binned to a resolution of 2.1 km s^{-1} ; marked velocities are expressed in km s^{-1} and relative to the LSR. The star velocity is $V_* = -26.5 \text{ km s}^{-1}$.

of both instruments in the uv-plane region where they overlap. Thanks to the Subcompact configuration, the SMA visibilities extended down to the physical size of the antennas, providing a comfortable range of overlap: from 6 m to 24 m. This allowed us in step (c) to discard the single-dish pseudo-visibilities with radii larger than 20 m, which critically depend on the beam pointing and shape, and are therefore less reliable. The amplitudes of the single-dish pseudo-visibilities were scaled by a factor 1.7 to match the azimuthally-averaged SMA amplitudes in the overlap region. No apodisation was applied during step (e), i.e. the SMA visibilities were processed with their natural weights; the weights of the single-dish pseudo-visibilities, on the other hand, were lowered to a constant value to avoid an undue widening of the synthesized beam.

The uv-plane coverage with the SMA and with ALMA is illustrated in Fig. 2. The mosaicing observing mode allows, in principle, for recovery of part of the visibilities for spacings < 6 m. However, since these have a low weight, the reconstruction of the SMA images remains problematic, particularly near the extended central source.

The final SMA and SMA+SD image datacubes are shown in Figs. 3 and 4 in the form of velocity-channel maps of velocity resolution 2.1 km s^{-1} . The angular resolution (synthesized beam HPW) is $3.7'' \times 3.0''$ (PA = -51°) for the SMA maps and $3.8'' \times 3.1''$ (PA = -51°) for the SMA+SD maps. The rms noise in the maps varies from $0.25 \text{ mJy beam}^{-1}$, in the region within $\pm 50''$ in Dec and $\pm 120''$ in RA from CW Leo \star , to $0.35 \text{ mJy beam}^{-1}$ at the map edges. The CO line emission shows a very strong source at the position of CW Leo \star . This source is so bright that it causes strong negative lobes in the dirty map at radii $r \leq 30''$, lobes that turned out impossible to clean despite the mosaicing observing mode, in view of the limited dynamic range of the SMA data. To obtain reliable images of this region, we have re-observed the central 1 arcmin with ALMA.

2.2. ALMA observations

The 1-mm ALMA observations (project code 2013.1.01215.S) were made with the 12-m array in the Compact configuration (Dec. 2014 and Jan. 2015, 32 antennas) and in the Extended

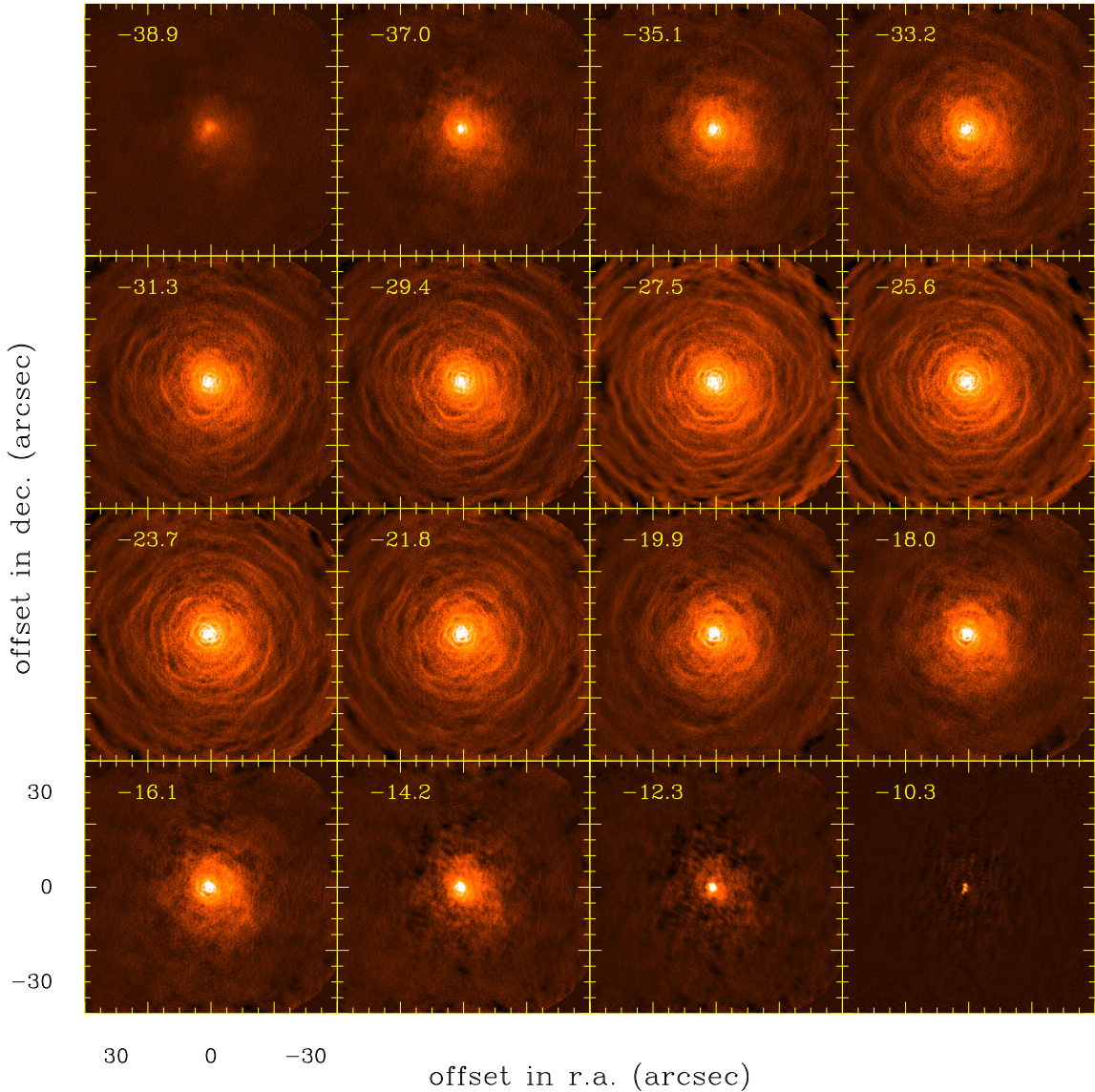


Fig. 5. Velocity-channel maps of the CO(2–1) line emission in the central $80'' \times 80''$ area of the IRC +10 216 envelope, observed with ALMA+SD at a spatial resolution of $0.35'' \times 0.33''$ (HPBW, PA = 38°). The spectra have been binned to a resolution of 1.9 km s^{-1} ; marked velocities are expressed in km s^{-1} and relative to the LSR. The star velocity is $V_* = -26.5 \text{ km s}^{-1}$.

configuration (June 2015, 39 antennas). Ganymede and the quasars 0854+2006 and J1008+0621 were observed on every track for flux and phase calibration. The baselines ranged from 12.7 m to 1569.4 m. The observing mode consisted of a 27-field mosaic with adjacent pointings spaced by $11.2''$ in RA and $12.9''$ in Dec, i.e. spaced by 0.42 and 0.48 times the 12-m antenna primary beam (HPBW $26.8''$ at the CO(2–1) line frequency). The mosaic covered a square area of $60'' \times 60''$ at full sensitivity, extending to $90'' \times 80''$ at 1/5th sensitivity. Besides CO(2–1), the usable band of the ALMA Band 6 receiver covered several molecular lines of interest, the most conspicuous being the three upper CN($N = 2-1$) fine structure (fs) components (around 226.9 GHz), both C_4H ($N = 24-23$) fs components (228.3486 and 228.3870 GHz) and, in the receiver upper-sideband, the CS($J = 5-4$) line (244.9350 GHz). Those were simultaneously observed with CO using several spectral correlator windows with different spectral resolutions. The channel separation for the CO, CN, C_4H and CS lines was 0.2 km s^{-1} , 0.3 km s^{-1} , 0.4 km s^{-1} and 0.6 km s^{-1} , respectively; most of the data presented here were binned to resolutions of 1 or 2 km s^{-1} .

One subband of the correlator was tuned to fully cover the 244.2–246.1 GHz sky frequency interval from the receiver upper sideband. The only truly strong line in this interval is the 244.935 GHz line of CS(5–4). After discarding the channels with CS emission, we used this subband to derive the continuum emission.

The data were calibrated through the ALMA/CASA pipeline. The resulting *uvfits* files were converted into the GILDAS uvt format and further processing was made with the GILDAS/MAPPING/MOSAIC software package. The process was similar to that just described for the SMA data: two CO(2–1) image datacubes were produced, one for ALMA data, the other for the merged ALMA plus SD data. The channel-velocity maps, binned to velocity resolutions of 1.9 km s^{-1} are shown in Fig. 5 for ALMA+SD CO and in Fig. 6 for ALMA C_4H . The synthesized HPBW is $0.34'' \times 0.31''$ (PA = $+36^\circ$) for the ALMA maps and $0.35'' \times 0.33''$ (PA = $+38^\circ$) for the ALMA+SD maps. The rms noise is 3 mJy beam^{-1} per 2 km s^{-1} channel and $50 \mu\text{Jy beam}^{-1}$ in the continuum 1.9 GHz subband. A comparison of the ALMA+SD map, smoothed to the resolution of the

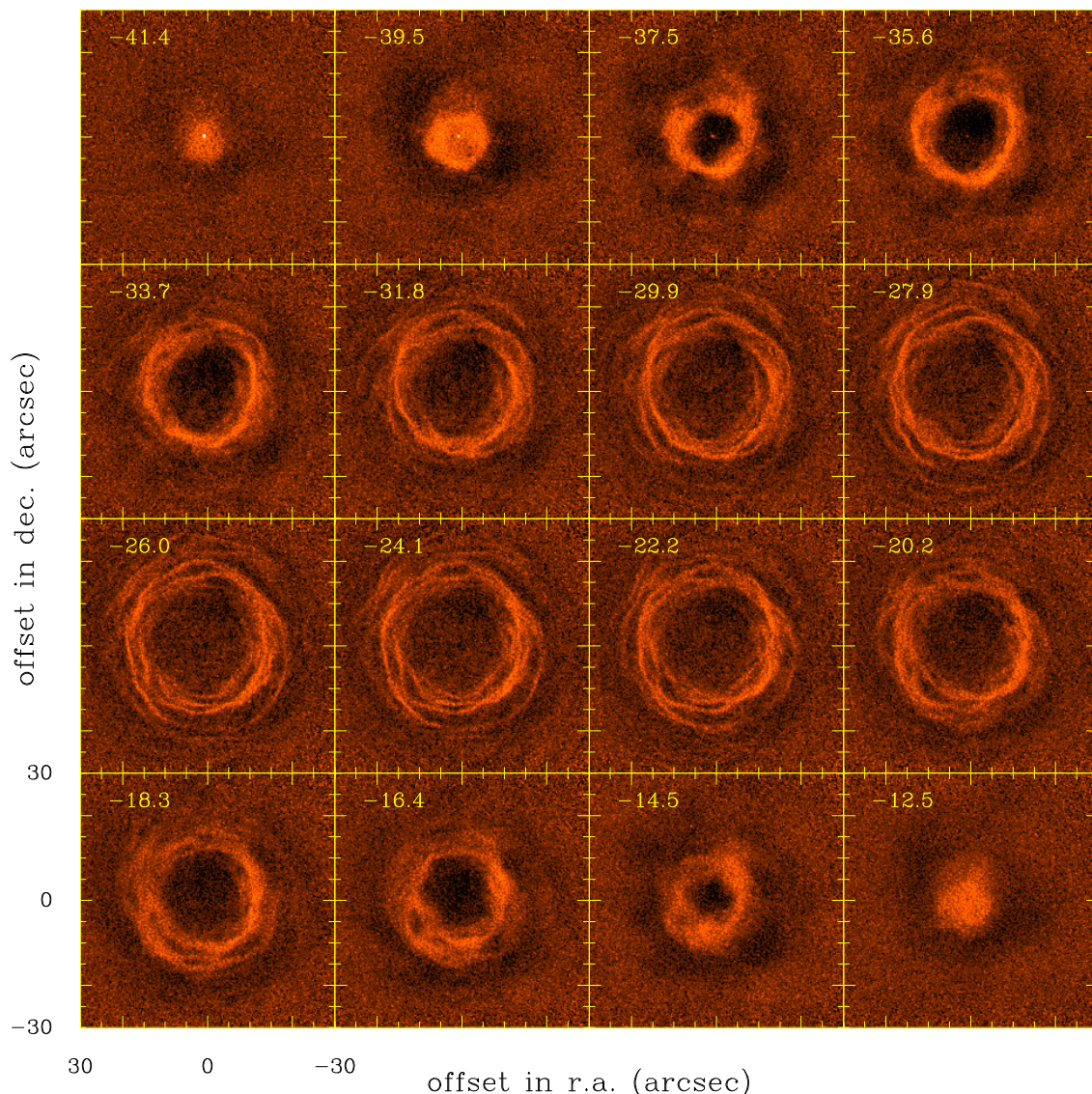


Fig. 6. Velocity-channel maps of the $\text{C}_4\text{H}(N = 24\text{--}23)$ line emission in the central $60'' \times 60''$ area of the IRC +10 216 envelope, observed with ALMA. The spectra have been binned to a resolution of 1.9 km s^{-1} ; marked velocities are relative to the LSR. The star velocity is $V_* = -26.5 \text{ km s}^{-1}$; velocities more positive or more negative correspond to the rear and front parts of the envelope, respectively.

SMA+SD map, shows the same bright structures than the latter, outside the innermost region ($r > 20''$).

The 3-mm ALMA observations (project code 2013.1.00432.S) were obtained in 2015 with the 12-m array in the Compact and Extended configurations. They consisted in a single pointing, centered on the position of the star in 2012.4 (see Table 1), and were part of a spectral survey covering the 3-mm atmospheric window. The field of view (half-power primary beam width) of the 12-m ALMA antennas at 115.5 GHz is $54''$. The 3-mm data were processed like the 1-mm data and similarly combined with 30-m SD data. The synthesized HPBW was $0.48'' \times 0.45''$ for the $\text{CO}(1\text{--}0)$ line. A thorough description of the spectral survey will be presented elsewhere (Cernicharo et al., in prep.).

2.3. IRAM 30-m single-dish telescope and PdBI observations

The $\text{CO}(2\text{--}1)$ 30-m SD observations were reported in Cernicharo et al. (2015). They mainly consisted of a fully sampled square map of size $480'' \times 480''$, plus 4 additional $240'' \times 240''$ maps centred at the corners of this square. All maps were

observed on-the-fly and a low order baseline was subtracted from each of the dumped spectra. The baseline subtraction removed the receiver instabilities, but also the continuum signal. The telescope radiation pattern mainly consists of a Gaussian main beam, of half-power width (HPBW) $11''$, plus a much wider error beam containing 25% of the total power. The contribution of the error beam was subtracted in the maps and analysis presented here. Figure 1 shows the emission seen by the 30-m SD telescope at the velocity of the star CW Leo \star . These observations have been used as short spacings for the SMA and ALMA $\text{CO } J = 2\text{--}1$ line data presented here.

Additional $\text{CO}(1\text{--}0)$ and $^{13}\text{CO}(1\text{--}0)$ observations, consisting of a fully sampled map of size $120'' \times 120''$, centred on the star, were made in the Fall 2015 with the 30-m telescope, as part of a spectral survey (Agúndez et al. 2017; Quintana-Lacaci et al. 2016).

Finally, fully sampled $120'' \times 120''$ maps of the $\text{C}_4\text{H}(24\text{--}23)$, $\text{CN}(2\text{--}1)$ and $\text{CS}(5\text{--}4)$ line emissions were carried out in December 2016 with the 30 m IRAM telescope. They provide the total flux and short spacings for the ALMA maps.

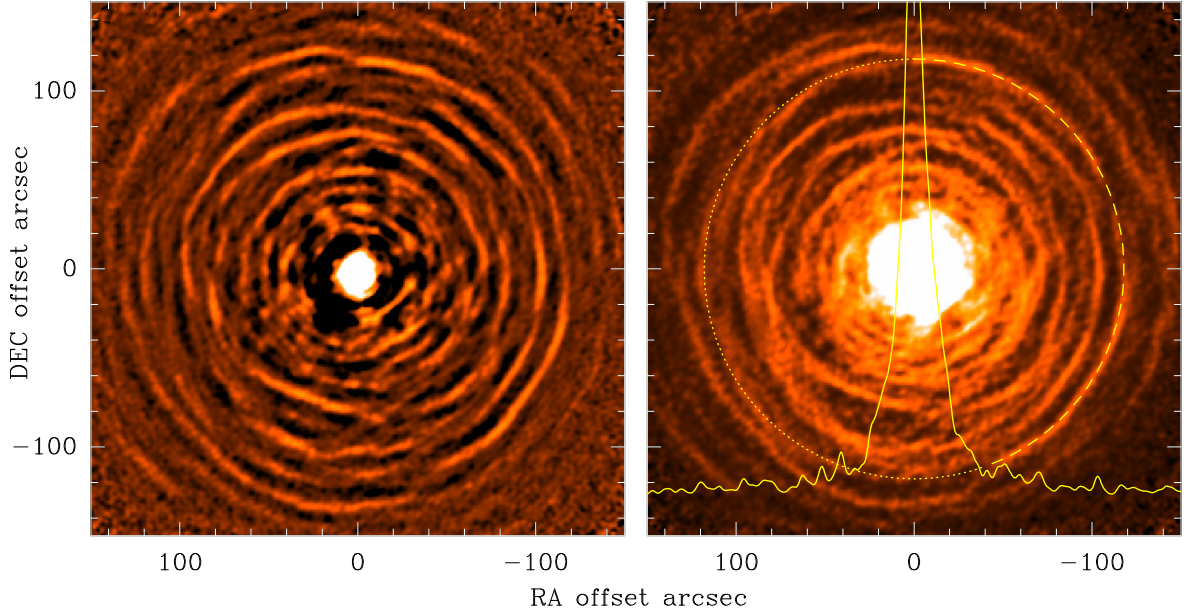


Fig. 7. Maps of the CO(2–1) line emission at the star velocity (-26.5 km s^{-1}) viewed by the SMA before (*left*) and after (*right*) inclusion of the 30-m single-dish short spacings. The yellow curve shows the intensity profile along an EW strip passing through the central star. Most of the bright CO arcs have circular shapes and denote the intersection of the meridional plane with thin spherical shells. The latter typically extend over several steradians, as illustrated by the arc at $r = 118''$ in the western half of the envelope (dashed yellow circle). The dense gas shell associated with this arc can be followed over π radians along the line of sight in Fig. 19.

Prior to the SMA and ALMA observations, we made preliminary CO(2–1) interferometric observations with the PdBI 6 antenna array. They consisted in a mosaic covering one quarter of a $60''$ -wide annulus of inner radius $50''$. The synthesized HPBW was $1.4'' \times 1.2''$ and the noise 30 mJy beam^{-1} in 3 km s^{-1} -wide channels. Since the same region was re-observed with the SMA with a higher sensitivity and denser uv plane coverage, the PdBI data will be used only in Sect. 3.1, when we compare the inner to the outer arc pattern.

3. Results

3.1. Gas distribution in the meridional plane

3.1.1. Outer envelope

As pointed out above, the outer envelope appears to be expanding with a constant velocity of 14.5 km s^{-1} and has a small ($<1 \text{ km s}^{-1}$) turbulence velocity, judging from the remarkably constant width of the molecular lines (we further discuss this point below in Sect. 4.1, when dealing with the 3D structure of the envelope). Each velocity-channel map (of e.g. Figs. 4 and 5) shows the emission from a conical sector (of opening θ and thickness $\delta\theta$), with its axis aligned to the line of sight to the star CW Leo \star (see Fig. A.1). The extreme velocities -40 km s^{-1} and -12 km s^{-1} correspond to the approaching and receding polar cones and caps, while the central velocity $V_* = -26.5 \text{ km s}^{-1}$ corresponds to a cut through the envelope at the star position; the CO envelope being roughly spherical, the $V_* = -26.5 \text{ km s}^{-1}$ map appears more extended.

Figure 7 shows an enlargement of the CO $V = -26.7 \text{ km s}^{-1}$ map before (*left panel*) and after (*right panel*) addition of the SD short spacings. Thanks to the filtering of the extended emission component by the interferometer, the left map shows more clearly the bright ringed structure noted in previous observations. The bright arcs, which trace dense shells of molecular gas in the outer envelope (see Cernicharo et al. 2015), appear far more

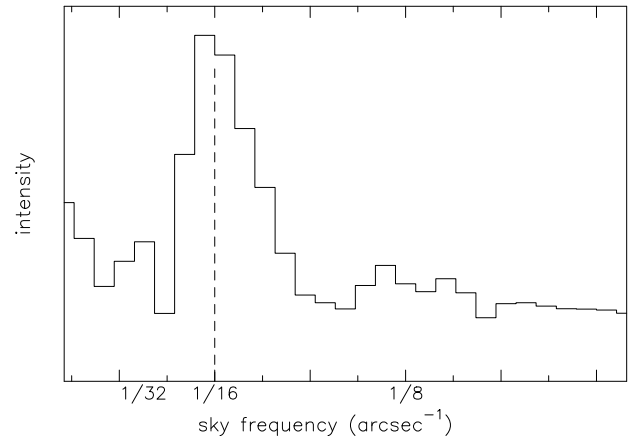


Fig. 8. Fourier transform of the azimuthally averaged CO(2–1) line brightness distribution for the W half of the envelope. Abcissa is spatial frequency in arcsec^{-1} .

clearly at the $3''$ resolution of the SMA than at the $11''$ resolution of the 30-m SD (Fig. 1). Surprisingly, they look almost circular and seem regularly spaced, except for three nearly straight segments in the SE quadrant. In contrast, the pattern in the inner $30''$ radius region appears confused in Fig. 7, due to artefacts in the image restoration process. We discuss the central region below.

We have analyzed the ring pattern in the outer envelope by azimuthally averaging the SMA map of Fig. 7 in the NW, NE, SE and SW quarters and by Fourier transforming the resulting 4 radial profiles from $r = 20''$ to $r = 150''$. Except for the SE quadrant, the FT shows a marked peak that corresponds to a period of $16''$ (Fig. 8), i.e. to a time lag of 700 yr for an expansion velocity of 14.5 km s^{-1} and a distance of 130 pc. Most of bright rings of the outer envelope can be fairly well fitted in each quadrant by circular arcs.

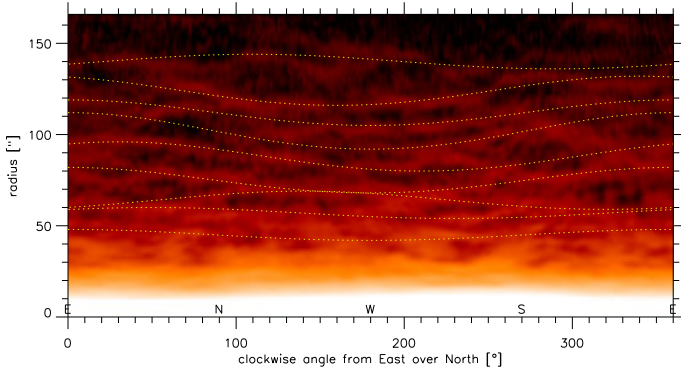


Fig. 9. CO(2–1) brightness distribution of Fig. 7 in polar coordinates and logarithmic scale. The yellow sinusoids traced over the brightest features correspond to slightly off-centred circles in the meridional plane.

The circular arcs are centred close to CW Leo★, albeit not exactly on. This was first noted by Guélin et al. (1993a), who studied the shape of the inner bright ring at $r \approx 15''$ appearing on the C₄H maps and found that it was centred a couple of arcsec NE of the star. They interpreted the offset as a drift of the dense shell, caused by an orbital motion of CW Leo★. The brightest arcs in Fig. 7 may be similarly fitted by circular arcs slightly offset; the offsets range between $2''$ and $10''$.

We note that the fits become poorer when replacing the circular arcs by segments of spirals with significant pitch angles. This is illustrated in Fig. 9, which shows the CO $V = -26.7 \text{ km s}^{-1}$ emission in polar coordinates. In that representation, an Archimedean spiral would appear as a tilted straight line. We observe instead 100–150°-long segments almost parallel the x -axis, bending up or down near their edges by up to $10''$, i.e. the signature of slightly off-centred circular arcs. The bending of several bright segments (e.g. at $r = 100''$ and $130''$) occur around angles of $170^\circ \pm 180^\circ$, implying an off-centering along the E-W axis. Globally, the offset appears to increase with radius.

3.1.2. Central region

The CO emission at the star velocity in the central part of the envelope is shown at different scales in the 3 panels of Fig. 10: *left frame* $380'' \times 380''$ SMA map with at its center the $90'' \times 80''$ 27 field mosaic ALMA map; *center frame* the ALMA map at an enlarged scale; *right frame* a zoom into the central $12'' \times 12''$ region of the ALMA map. No SD data has been added in this figure.

The remarkable periodicity of the bright arcs in the outer envelope appears to break down within an arcmin of the star. This is not just an effect of the tenfold increase in angular resolution and sensitivity. Indeed, closer than $50''$ from the star, the SMA map shows the same contracted arc pattern as the ALMA data, smoothed to the $3''$ SMA resolution; similarly the arc pattern observed between $50''$ and $110''$ E of CW Leo★ with PdBI, smoothed to $3''$, is the same as that in (Fig. 7).

Between $r = 10''$ and $r = 40''$, the spacing between the brightest arcs is $\approx 10''$ in the NW quadrant and further decreases to $\approx 2''$ closer to the star. The spacing is even smaller in the opposite (SE) quadrant, possibly the effect of a NW drift of the arc centers. We note that the innermost arcs in Fig. 10 seem to form a series of off-centred rings, rather than a single regular spiral. This is illustrated on the right frame by the fit to the inner arc pattern of 3 circles with radii $2.3''$, $3.3''$ and $5''$, respectively

centred at $(0.35'', 0.45'')$, $(-0.6'', 0.3'')$ and $(-0.8'', 0.5'')$ from the star. We note that the arc centres seem to drift to the W with increasing radius, i.e. with the arc age. The arcs are fully resolved with the $0.3''$ ALMA beam. They appear as tangled filaments, some of which are kinked or show bridging branches.

The appearance of the dense shells in the CO(2–1) line, particularly in Fig. 4, is confused by the bright CO source around the star and by the CO emission in the intershell region. In order to have a clearer view of the inner shells, we have turned to two radicals, namely C₄H and CN, known to form far from the star. The C₄H($N = 24-23$) and CN($N = 2-1$) line frequencies are close enough to that of the CO(2–1) line, and were observed simultaneously with the ALMA receiver.

Figure 6 shows the velocity-channel maps of the upper frequency component of the C₄H ($N = 24-23$) line doublet, observed with ALMA. The continuum emission has been removed. As expected, no emission is detected near the star, except for foreground and background emission at terminal velocities (near -12 km s^{-1} and -40 km s^{-1}). We also note a point-like source near -38 km s^{-1} of width $\approx 6 \text{ km s}^{-1}$ characteristic of vibrationally excited lines, that can be assigned to Si³⁴S $\nu = 1 J = 13-12$ at $\nu = 228\,399.382 \text{ MHz}$. Lines from SiS and its isotopologues involving vibrationally excited states from $\nu = 1$ up to $\nu = 10$ have been detected with ALMA by Cernicharo et al. (2013) and in the infrared by Fonfría et al. (2015).

It was previously noted by Guélin et al. (1993a) that the C₄H emission is essentially confined to a thick shell extending from $r = 10''$ to $r = 25''$; the brightest contours at the star velocity ($V_* = -26.5 \text{ km s}^{-1}$) trace a thick circular ring centred $2''$ NE of the star. With the $0.3''$ ALMA beam, each shell is resolved into $\approx 1''$ -thick arcs with different radii and different centers of curvature. The outermost arc to the SW, which on the -26 km s^{-1} map may be interpreted as the onset of a spiral, rather appears as a circle centred at $(0.6'', -2.6'')$ on the adjacent -24 km s^{-1} and -22 km s^{-1} velocity-channel maps (see Fig. 6).

This arc structure is not specific to C₄H, but also found for the CN(2–1) line emission. Figure 11 shows the C₄H($N = 24-23$) and CN($N = 2-1$) channel-velocity maps at $V_* = -26.5 \text{ km s}^{-1}$. CN emission extends further out than the C₄H emission, but, although much stronger, is not observed at smaller radii, hence does not appear earlier than C₄H. Within the radius range where all three species are detected, the correlation between the CN, C₄H and CO bright arcs is striking: this is illustrated in the figure by the superimposition of the CN $0.025 \text{ Jy beam}^{-1}$ brightness contour (cyan color contour) on the C₄H and CO maps. As noted above, the bright central arcs may be fitted by circular arcs whose centers of curvature are offset by a few arcsec from the star.

Figure 13 shows the CO and CN (2–1) line brightness contours at the star velocity superimposed on the VLT image of the interstellar light (V band) scattered by the dense shell dust grains (Leão et al. 2006). Again, the 3 tracers show very similar intensity profiles along the arcs (it should be noted that the imprint of a number of stars has been removed from the VLT image so that some areas are artificially dim – see Leão *ibid.*). The agreement between CO and dust is not surprising, as the scattered light is enhanced where the line-of-sight is tangent to the dense shells, i.e. near the meridional plane. As expected, the optical arcs are somewhat broader and, at places, lie slightly inside the CO arcs.

The similarity between the C₄H and CN line brightness distributions, as well as the line brightness distributions of many other C-chain molecules and radicals (C₂H, C₆H, HC₅N, MgNC,...), was already noticed in lower resolution interferometric maps by Guélin et al. (1993a) and Lucas & Guélin (1999),

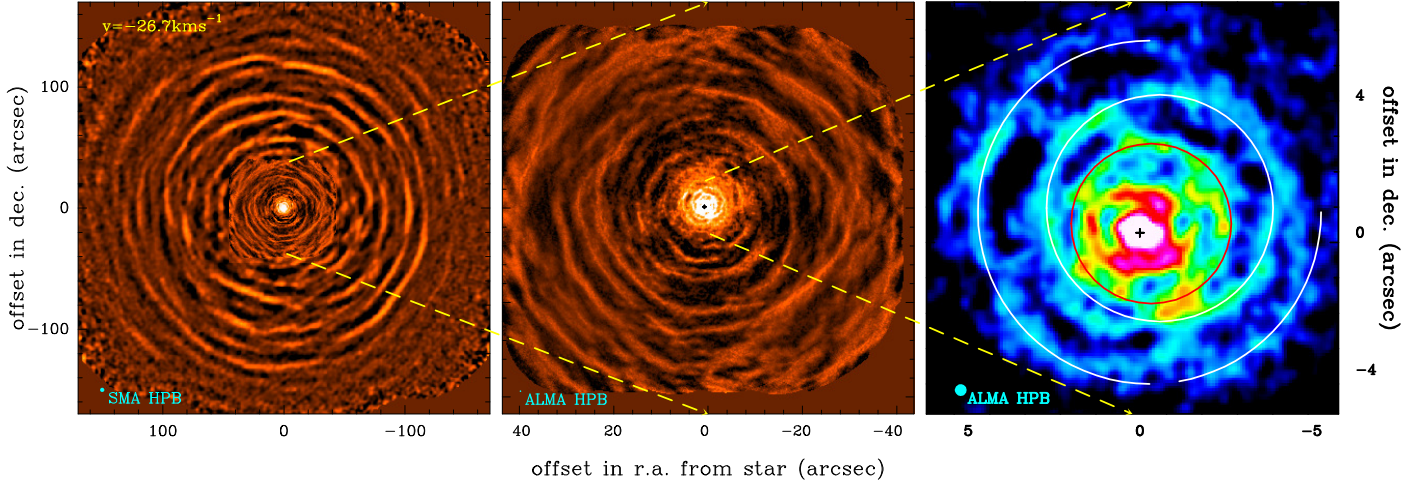


Fig. 10. CO(2–1) emission at the star velocity ($V_* = -26.5 \text{ km s}^{-1}$) at different scales: *left frame*: $380'' \times 380''$ SMA map (HPBW $3''$) with, at its center, the $90'' \times 80''$ 27 field mosaic ALMA map; *center frame*: ALMA map (HPBW $0.34'' \times 0.31''$) at an enlarged scale; and *right frame*: zoom on the $12'' \times 12''$ inner region of the envelope. No SD data has been added. The color code in *the right panel* is chosen to underline the bright arcs. The circles illustrate a possible fit of the arc-like features with slightly off-centred circular arcs. The blue dots show the SMA and ALMA half-power beam widths. Position (0, 0 black cross) corresponds to the star $09^{\text{h}}47^{\text{m}}57.4492^{\text{s}} 13^{\circ}16'43.884''$ – see Table 1.

who pointed out it seems to contradict the standard formation scheme of those species, namely carbon-chain growth initialized by the photodissociation of acetylene. The neutral-neutral reactions involved being relatively slow, one may expect the species to appear sequentially at different radii. The high resolution maps of Fig. 11 show that the apparition of the CN and C_4H emissions coincide in the inner envelope to better than $1''$, i.e. a few tens of years, setting stringent constraints on the chemistry. This question has been addressed by Cordiner & Millar (2009) and, more recently, by Agúndez et al. (2017) who stress the role of fast photodestruction reactions in shaping up the localisation of C-chains in the envelope.

3.2. Continuum emission

The 1-mm continuum emission from the envelope has been previously mapped at a resolution of $11''$ (HPBW) with the IRAM 30-m telescope equipped with a bolometer (Groenewegen et al. 1997). The authors reported a broad, centrally peaked emission extending up to $r \approx 40''$ from the star, an extension polluted by the telescope error beam response and by line emission. The bolometer band, centred at 240 GHz, has an equivalent bandwidth of ≈ 70 GHz and covers very many molecular lines, some of which are very strong (CO, SiO, CS, HCN, HC_3N ...). As to the 30-m telescope observations discussed in Sect. 2.3, they were carried out with HERA, a heterodyne receiver too unstable to yield accurate continuum information in total power mode.

The interferometric SMA and ALMA observations have both the stability and the resolution required to measure weak continuum signals and discard the line emission. However, they partly filter out the extended emission and accurately show only structures smaller than $10''$ – the shortest spacings observed with the SMA and ALMA were 6 m and 12.7 m, respectively, which, despite the mosaicing observing mode, implies partial loss of smooth continuum features broader than $12''$ (ALMA) and $25''$ (SMA).

The continuum emission detected by both interferometers consists of a compact central source and a clumpy halo. A Gaussian fit of the compact source in the ALMA uv visibilities yields a peak flux of 0.33 Jy and a FWHM of 0.22 ± 0.01 arcsec. The

Table 1. Quoted error is 1σ for each coordinate.

Epoch	Freq. GHz	HPBW ''	RA (J2000) h:m:s	Dec (J2000) ° : ''	1σ mas	Ref.
2015.6	245	0.3	09:47:57.4492	13:16:43.884	4	[1]
2015.92	650	0.3	09:47:57.4553	13:16:43.749	20	[2]
2012.29	260	0.6	09:47:57.446	13:16:43.86	30	[3]
2006.16	43	0.04	09:47:57.4255	13:16:43.815	10	[4]
1993.07	22.5	0.1	09:47:57.39	13:16:43.63	20	[5]

References. [1]: this work; [2]: Decin et al. (2015); [3]: Cernicharo et al. (2013); [4]: Menten et al. (2012); [5]: Menten et al. (2006).

brightness temperature of the optically thin continuum emission is >100 K: obviously, the compact source corresponds to the hot dust formation zone.

CW Leo \star is known from VLBA 7-mm observations to have a proper motion of 35 mas yr^{-1} in the NE direction (PA = 70°) (Menten et al. 2012), which translates in a total motion of $\sim 0.1''$ during the 3-yr duration of our SMA and ALMA observations. The position of the star in June 2015, identified as the center of the bright 0.2 arcsec 245 GHz continuum source in our extended configuration ALMA observations, is $09^{\text{h}}47^{\text{m}}57.4492^{\text{s}} 13^{\circ}16'43.884''$. It is adopted as the reference position for the maps in this article. In Table 1, it is compared to other accurate measurements made with ALMA and the VLA. We note that the 0.3 Jy continuum source detected at 245 GHz at the center of the map, which consists of the star plus surrounding hot dust, is not quite axisymmetrical. Therefore, its position slightly varies with the HPBW.

Figure 12 shows the radial profile of the azimuthally averaged continuum halo, compared to the azimuthally averaged CO(2–1) emission in the ALMA central velocity map. The clumpy continuum halo appears as a series of ripples of decreasing intensities, e.g. peaking near 3, 6 and 9 arcsec. These ripples coincide in radius with ripples on the CO profile, which trace the bright CO arcs smeared by the azimuthal average. The ripples in Fig. 12 show that the innermost CO arcs are detected in the continuum, although they are hardly visible on

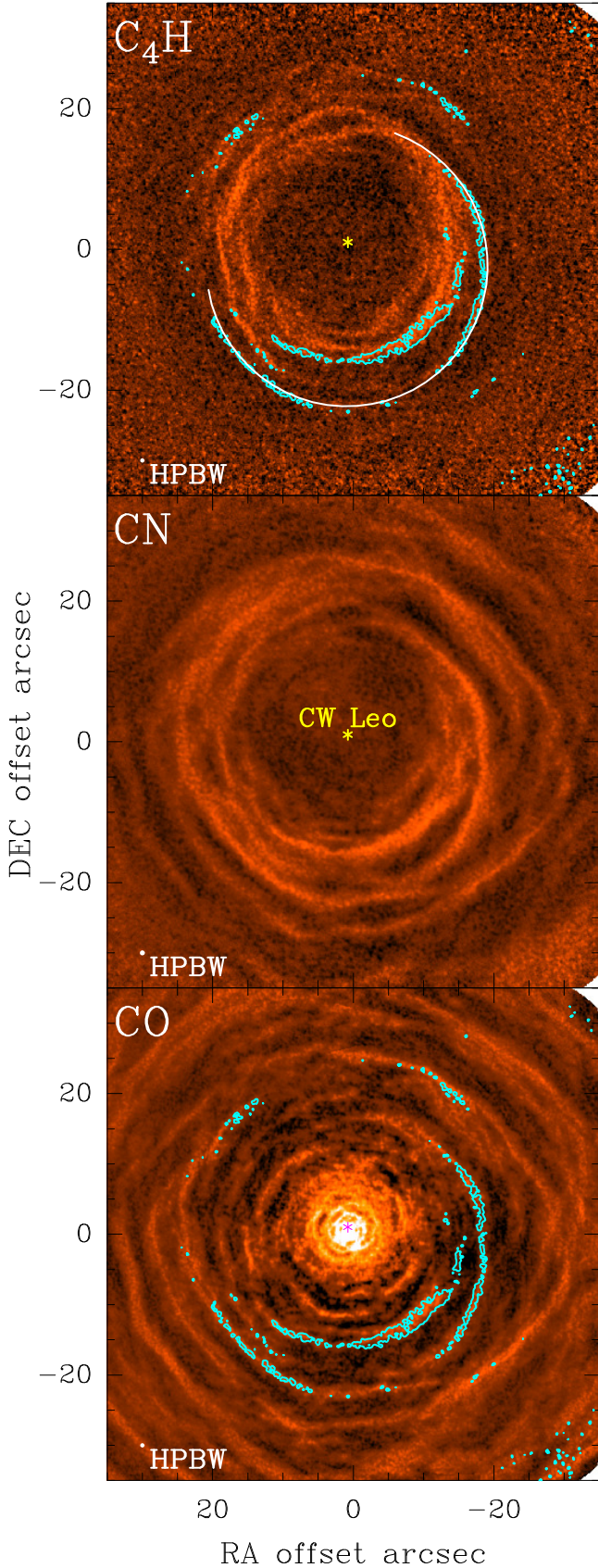


Fig. 11. $C_4H(24-23)$ and $CN(2-1)$ emissions at the star velocity ($V_* = -26.5 \text{ km s}^{-1}$), observed with ALMA (HPBW $0.34'' \times 0.31''$), compared to the $CO(2-1)$ emission. The cyan color contours correspond to the $0.25 \text{ Jy beam}^{-1}$ level from the CN map. The star indicates the position of CW Leo \star . The white circular arc on the upper frame is a fit to the bright southern arc; it is centred $0.6''$ E, $2.6''$ S of CW Leo \star .

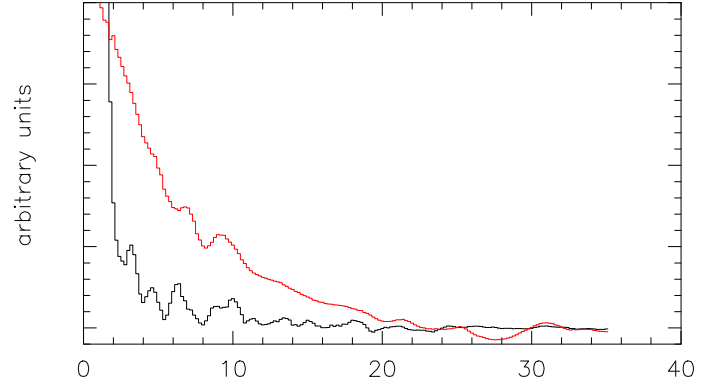


Fig. 12. Radial profile of the azimuthally averaged 1-mm continuum emission (black) and $CO(2-1)$ emission (red). X axis is radius in arcsec, Y axis intensity in an arbitrary scale. The bumps correspond to segments of bright off-center arcs.

the unsmoothed continuum map. After cautioning that the extended CO and continuum emissions may be unequally filtered out by the ALMA interferometer, we note that the CO ripples, expressed in Jy km s^{-1} , are a factor of ≈ 10 stronger than the continuum flux density, expressed in Jy. This factor is comparable to the ratio of the velocity-integrated $CO(2-1)$ line flux $\int S_{CO} dv$ to the 1-mm continuum flux S_ν observed in the cold interstellar clouds: ≈ 8 (see e.g. Guélin et al. 1993b).

4. 3D reconstruction of the dense shells

4.1. Position-Velocity diagrams

The discussion in Sect. 3 was mostly based on the maps at the envelope systemic velocity and only dealt with the line brightness in the meridional plane perpendicular to the line-of-sight. We now analyze the full range of velocities to recover the gas distribution along the line-of-sight. Let us first consider the position-velocity diagrams along narrow slits at position angles (PA) 0° , 45° and 90° and passing through the star CW Leo \star .

Figure 14 shows the position-velocity (PV) diagram of the $CO(2-1)$ emission in the outer envelope, as traced by the SMA+SD observations along a $3''$ -wide, $220''$ -long slit, oriented NS at the right ascension of the star. The central part of the graph ($-40'' < r < +40''$) is heavily saturated due to the bright CO pedestal. PV diagrams of that central region, based on the ALMA data, are shown in Figs. 15 and 16. In all these figures, the dashed horizontal lines correspond to $-26.5 \pm 15 \text{ km s}^{-1}$, i.e. to the terminal velocities for an expansion velocity of 14.5 km s^{-1} , plus half the $w = 1 \text{ km s}^{-1}$ channel-width. It is striking to see how sharply the CO emission cuts-off at the redshifted terminal velocity (the bright ridge near $\Delta\delta \approx 0$ on the SMA+SD map is residual continuum emission from the hot dust-forming region). Note that the CO emission vanishes $\approx 2 \text{ km s}^{-1}$ earlier at blueshifted velocities, because the cold, incoming foreground gas absorbs the bright emission from the warm inner layers; we show below in Fig. 17 that the cut-off occurs symmetrically at $\Delta V \pm 14.5 + w/2 \text{ km s}^{-1}$ for the optically thin C_4H emission.

On the CO PV diagrams (Figs. 14 to 16), the dense gas shells appear as bright elliptical arcs, as expected for *spherical shells expanding at a constant velocity*. The white ellipses on the figures correspond to spherical shells of radii $16''$, $32''$, $48''$, $78''$, $99''$ and $107''$, centred within $2''$ from the star and radially expanding at $V_{\text{exp}} = 14.5 \text{ km s}^{-1}$. Clearly, there

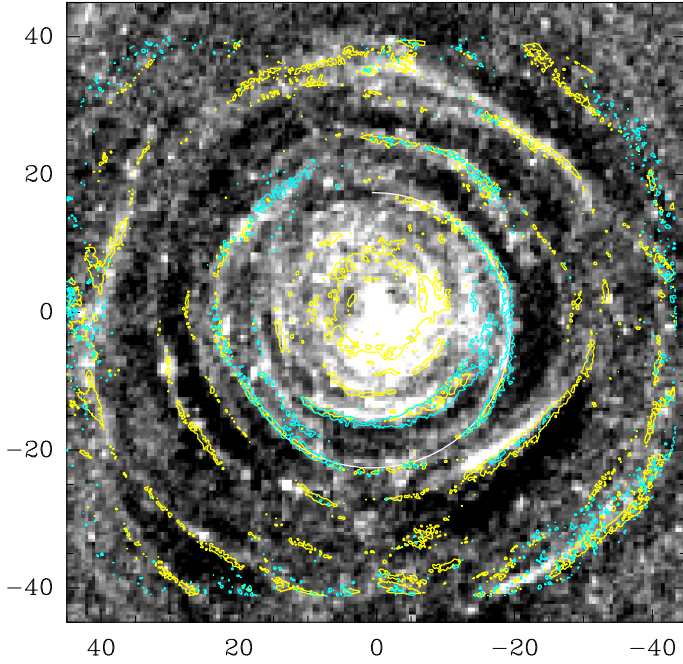


Fig. 13. Selected CO yellow and CN cyan color line brightness contours at $V_* = -26.5 \text{ km s}^{-1}$, superimposed on the VLT image of scattered V light of [Leão et al. \(2006\)](#). The white circle of radius $20''$ is centred at $0.6''\text{E}$, $2.6''\text{S}$ from CW Leo \star . Coordinates are RA and Dec offsets in arcsec.

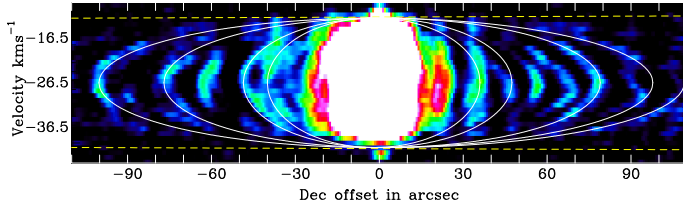


Fig. 14. Position-velocity diagram of the CO(2–1) emission, as traced by the SMA+SD observations, along an $3''$ -wide $220''$ -long slit oriented NS at the right ascension of the star ($13\text{h}:16\text{m}:43.9\text{s}$). The central region of the graph ($-40'' < r < +40''$) is heavily saturated. The dense shells seen in Fig. 7 take here the form of elliptical arcs. The white ellipses correspond to spherical shells of radii $38''$, $48''$, $78''$, $99''$, $107''$, centred within $2''$ from the continuum peak and in radial expansion at a velocity of 14.5 km s^{-1} .

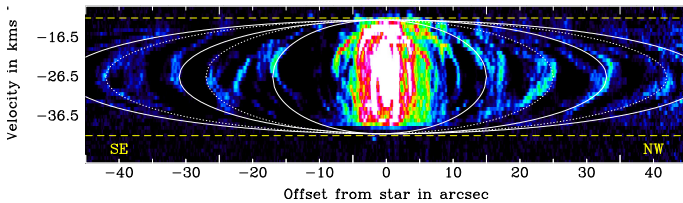


Fig. 15. Position-velocity diagram of the CO(2–1) emission, as traced by ALMA observations, along an $0.4''$ -wide $100''$ -long SE-NW oriented slit (PA = 45°) passing through the star. The dense shells seen in Fig. 7 appear as bright elliptical arcs. The white ellipses correspond to shells of radii $16''$, $32''$, $42''$, $48''$, centred within $2''$ from the continuum peak and in radial expansion at a velocity of 14.5 km s^{-1} .

are more bright arcs than shown ellipses in the figures and only parts of the model ellipses show bright emission, but overall the agreement between observations and a series of quasi-regularly spaced shells is remarkable. All bright arcs appear to converge toward the terminal velocity at the star position, which implies

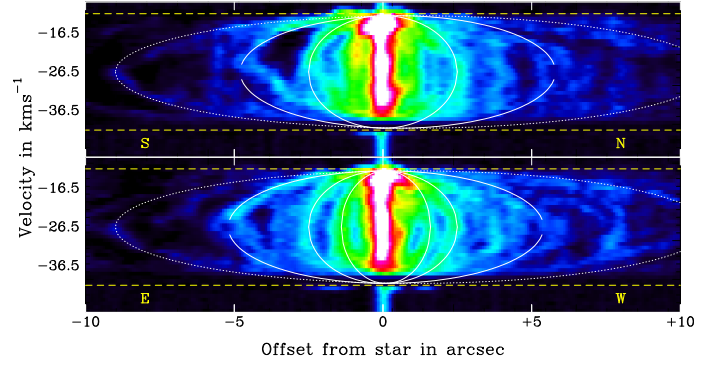


Fig. 16. Position-velocity diagram in the central region: the CO(2–1) emission, as traced by ALMA observations, along two $0.4''$ -wide $20''$ -long slits, respectively oriented NS and EW, and passing through the star. The dense shells seen in Fig. 7 appear as bright elliptical arcs. The white ellipses correspond to shells of radii $1.5''$, $2.5''$, $5.5''$, $10''$, centred within $0.1''$ – $1''$ from the continuum peak and in radial expansion at a velocity of 14.5 km s^{-1} .

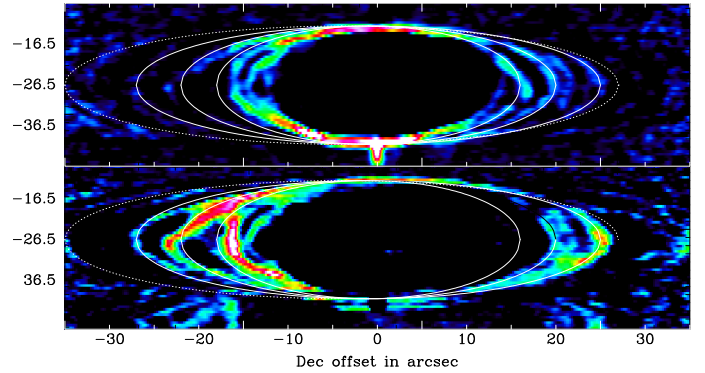


Fig. 17. Position-velocity diagrams of the $\text{C}_4\text{H}(N = 24\text{--}23)$ (top) and CN ($2_{032} - 1_{021}$) (bottom) line emission along a $1''$ -wide NS slit at the right ascension of the star ($09^{\text{h}}47^{\text{m}}57.45\text{s}$). The shells in Fig. 11 where C_4H is detected appear as bright elliptical arcs. The white/black ellipse corresponds to shells of radii $17''$, $21''$, $26''$ and $31''$ centred $1''\text{N}$ from the star ($4''\text{N}$ for the $31''$ shell) and in radial expansion at a velocity of 14.5 km s^{-1} . Note that the CN ($2_{032} - 1_{021}$) line shown here is blended by two weaker hfs components, ($2_{032} - 1_{022}$) and ($2_{033} - 1_{023}$), respectively 11.5 and 16.3 MHz higher in frequency. Those appear on the graph as ghosts of the brightest component shifted by -15.2 and -21.6 km s^{-1} .

that the expansion along the line of sight is uniform *and* that the gas turbulent velocity is small. It should be noted that the dark vertical lane at $\Delta\delta = 28''$ in Fig. 14 is an artifact caused by a negative lobe in the SMA map resulting from the limited uv-plane coverage. The lane is not present on the ALMA image, which has a higher fidelity.

The shell morphology is further illustrated in the PV diagram of Fig. 17, which presents the C_4H and CN emission along an NS oriented slit (very similar diagrams are observed for the corresponding EW slits). The bright arcs closely follow the model ellipses, $V(x) = V_{\text{exp}} \cdot \cos(\arcsin(x/R))$, where x is the offset and R the radius of the radially expanding spherical shell. We note that the trace of an oblate shell, resulting from addition of radial components orthogonal to the line-of-sight, would remain closer to the terminal velocity at low radii and fall off more briskly near the shell radius, i.e. would be more boxcar shaped. The thinness of the arcs around the star position is striking, allowing us to set an upper limit to the turbulent velocity V_{turb} of 0.6 km s^{-1} .

4.2. Spherical deprojection of the outer envelope

We thus adopt in the following a uniform expansion velocity of $V_{\text{exp}} = 14.5 \text{ km s}^{-1}$ and neglect turbulent motions. This enables us to extract from the position-velocity CO datacubes, XYV , a 3-dimensional (3D) spatial representation of the envelope and its dense shells, XYZ . Two different approaches, respectively dubbed *Non-iterative* and *Iterative*, were used for this 3D reconstruction. They are described in Appendix A together with comparative tests on envelope models. Both yield very similar results, though the iterative method images are less noisy and trace the arcs closer to the star, at the expense of degraded angular resolution and of tight spherical boundaries. For directions close to the center of expansion, i.e. CW Leo★, the line of sight velocity component comes to be degenerated. This, and the resulting increase of the CO(2–1) line opacity, prevents us from localizing the gas cells along the line of sight in the approaching and receding polar caps.

The results of the 3D reconstruction of the envelope, based on the SMA+SD data, are presented in Figs. 18 for the non-iterative method and in Fig. 19 for the iterative method. In both figures, the displayed frames show the reconstructed CO(2–1) line brightness distribution for 8 constant declination cuts parallel to the line-of-sight (Z axis). The planes are separated by $42''$ in declination (Y axis) and are located symmetrically with respect to CW Leo★.

The bright dense shells appear in both figures as red or yellow arcs, superimposed on a blue background. Black areas mark the regions where deprojection was not possible because, either the line opacity is large, or the velocity is degenerate along the line of sight. Both conditions are met near the terminal velocities for the lines of sight close to CW Leo★. Moreover, at all velocities, the emission at very small radii is dominated by the hot gas acceleration region, where our model of uniform expansion breaks down, making the deprojection codes ineffectual.

The great similarity of the images derived by two independent methods gives us confidence that the deprojected XYZ representation of the envelope is unequivocal and correct.

Like the bright arcs in the plane of the sky (Fig. 7), the arcs on the maps in Figs. 18 and 19 are close to circular and extend symmetrically in both directions along the line-of-sight. In frames $-63''$ and $+63''$, which are less affected by velocity degeneracy or by too weak a signal, the arcs form complete circles. The yellow circles, which mark the plane intersections with a sphere of radius $118''$, illustrate this point.

Most bright arcs can be followed when we rotate the panel planes around the line-of-sight by 90 degrees, i.e. until the cuts are oriented NS, instead of EW. We thus conclude that the dense shells, traced by CO in the outer envelope, have spherical or near-spherical shapes and that the envelope is not manifestly oblate.

4.3. Physical conditions and mass loss rate

We derive the physical conditions in IRC +10 216 through a comparison of the $^{12}\text{CO}(2-1)$, $^{12}\text{CO}(1-0)$ and $^{13}\text{CO}(1-0)$ or $^{13}\text{CO}(2-1)$ line intensities. This was done for the outer envelope in our previous study (Cernicharo et al. 2015), after averaging the line intensities over concentric rings of width $10''$. The lines were found to be subthermally excited at radii $r \geq 40''$ and the azimuthally-averaged $^{12}\text{CO}(2-1)$ line opacity τ was found in the range 2–4; the ^{13}CO lines are optically thin everywhere ($\tau < 0.1$). The gas kinetic temperature was found to decrease from $T_{\text{gas}} = 20 \text{ K}$ at $r = 40''$ to $\approx 15 \text{ K}$ at $r \geq 60''$ and the

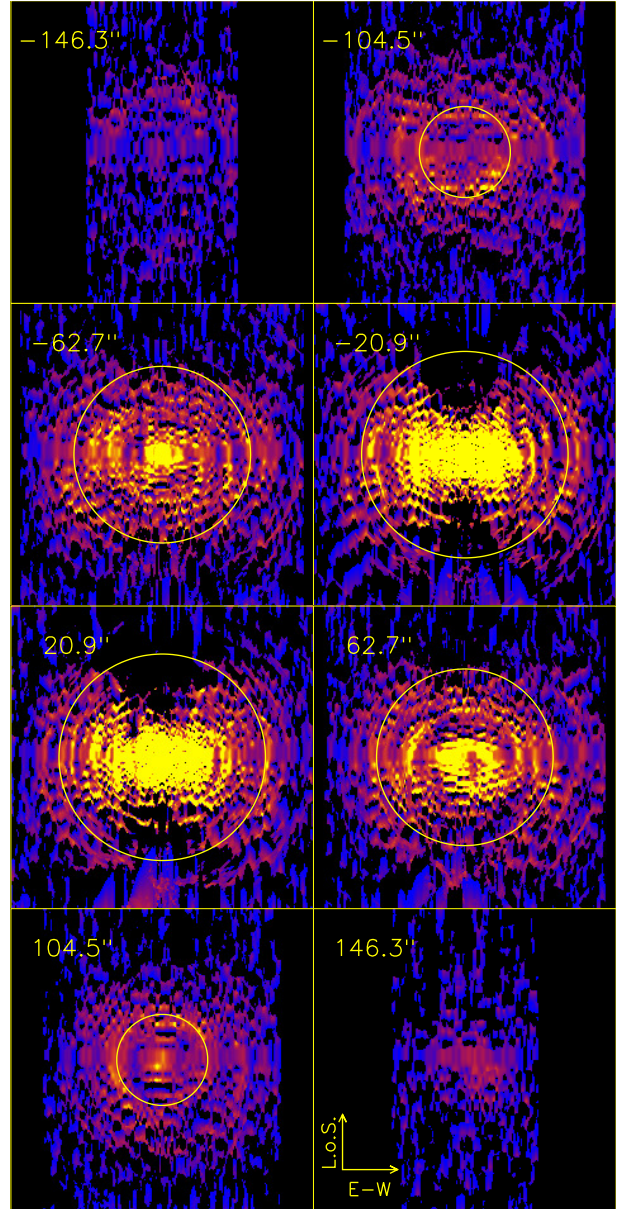


Fig. 18. Reconstructed images of the CO shells using the non-iterative method. The images correspond to slices along 8 horizontal planes parallel to the line-of-sight (X -axis runs from E to W and Y -axis along l.o.s.). The slices are spaced by $42''$; the star position corresponds to plane 0. Image sizes are $336'' \times 336''$. The approaching and receding halves of the envelope are down and up, respectively. Intensity scales are identical for all images (blue= dim, yellow= bright). The areas where reconstruction was not possible, due to velocity degeneracy or to too weak signals, are in black. The yellow circles mark the intersection with the planes of a sphere of radius $118''$.

gas density to decrease from $n_{\text{H}_2} = 5 \times 10^3 \text{ cm}^{-3}$ at $r = 40''$ to $1.2 \times 10^3 \text{ cm}^{-3}$ at $r = 80''$. The latter values, coupled to a fractional abundance $[^{12}\text{CO}]/[\text{H}_2]$ of 6×10^{-4} , imply an average mass loss rate $\dot{M} = (2-4) \times 10^{-5} M_{\odot} \text{ yr}^{-1}$ from 3400 yr ago to 1700 yr ago.

4.3.1. Rotational and kinetic temperatures

We resume this analysis for the central region, using the 1-mm and 3-mm ALMA+SD data described in Sect. 2, more particularly the velocity-channel maps at the envelope systemic velocity

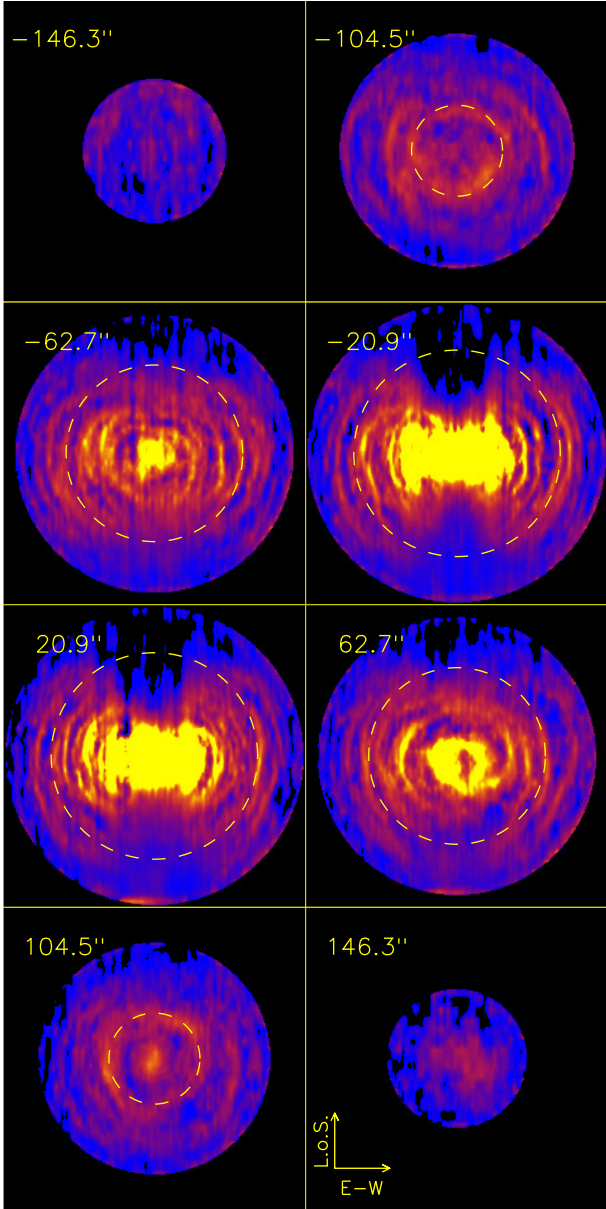


Fig. 19. Same as Fig. 18 for the iterative method (see text).

$V_* = -26.5 \text{ km s}^{-1}$. The latter provide direct information on the physical conditions throughout the meridional XY plane.

The $^{12}\text{CO}(2-1)$ ALMA+SD velocity-channel cube (1.9 km s^{-1} -wide channels) was first smoothed to the angular resolution of the $^{12}\text{CO}(1-0)$ cube ($0''.48 \times 0''.45$ – see upper frame of Fig. 20). Then, the central ($V_* = -26.5 \text{ km s}^{-1}$) velocity-channel maps of $^{12}\text{CO}(2-1)$ and $^{12}\text{CO}(1-0)$ were azimuthally averaged over $0''.53$ -thick concentric rings centred on CW Leo \star . This allowed us to derive the radial profiles of the

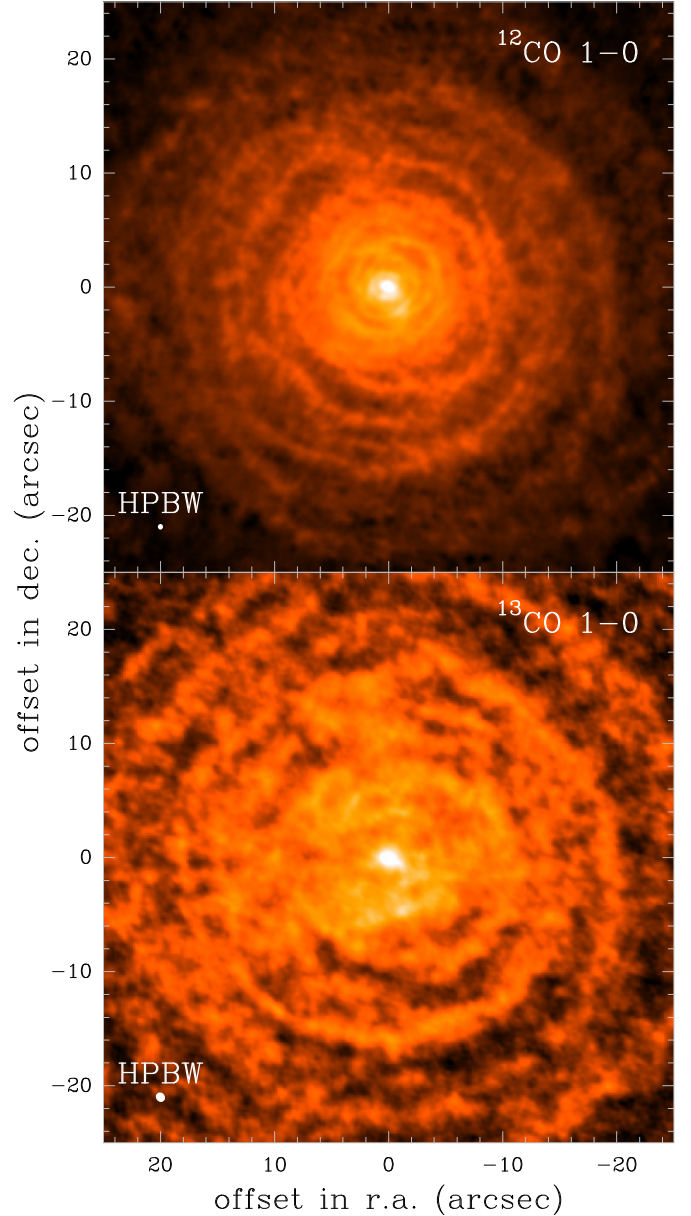


Fig. 20. $^{12}\text{CO}(1-0)$ (upper frame) and $^{13}\text{CO}(1-0)$ (lower frame) line brightness distributions at the envelope systemic velocity ($V_* = -26.5 \text{ km s}^{-1}$) for the ALMA+SD data. The synthesized beam half-power width, ($0''.48 \times 0''.45$) in the upper frame, has been degraded to ($0''.86 \times 0''.76$) for the rare isotopomer line.

$^{12}\text{CO}(2-1)$ peak line intensity, as well as of the $R_{21} = ^{12}\text{CO}(2-1)/^{12}\text{CO}(1-0)$ line brightness temperature ratio, throughout the $\approx 50''$ central region Fig. 20).

From the R_{21} radial profiles, we derive the rotation temperature profile T_{rot} , which represents the kinetic temperature T_k under the assumption that the low J ^{12}CO levels are at LTE. In Fig. 21, the ^{12}CO data set was completed in the inner $r \leq 1''$ region using the rotational temperatures derived by Fonfría et al. (2015, 2017) from ro-vibrational SiS and C_2H_4 lines.

The T_{rot} plot shows at $r \approx 15''$ ($\approx 750 R_*$ or $2.8 \times 10^{16} \text{ cm}$) a change in dependence on the distance from the star. At lower radii, T_{rot} closely follows a power-law $T_{\text{rot}} = (256.9 \pm 1.5)(r/0.8)^{-(0.675 \pm 0.003)} \text{ K}$, where r is expressed in arcsec. Beyond $r = 15''$, T_{rot} remains around 35 K.

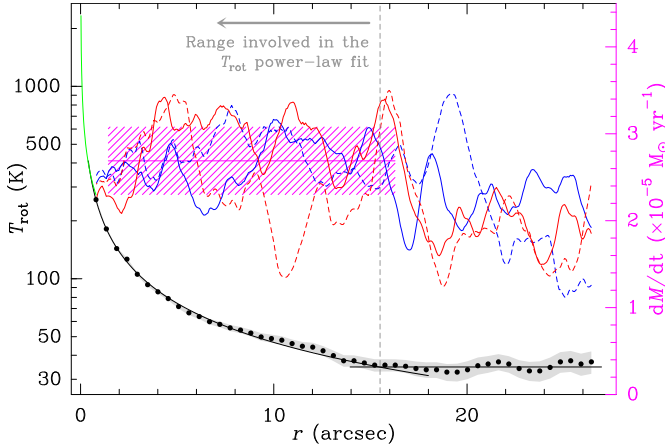


Fig. 21. Rotational temperature and mass-loss rate throughout the inner 50'' of the CSE. The rotational temperature (black dots) was derived from the $^{12}\text{CO}(2-1)/^{12}\text{CO}(1-0)$ ratio averaged in concentric rings centred on the star. The green curve is the kinetic temperature close to the star calculated from results of previous works. The grey accounts for the 1σ error interval of the rotational temperature. The vertical dashed grey line indicates the distance from the star where the rotational temperature changes its behaviour ($\approx 15''$). The black continuous lines are the fits to the data set up to $15''$ ($T_{\text{rot}} \propto r^{-0.68}$) and beyond ($T_{\text{rot}} \approx 35$ K). The thin colored lines represent the mass loss rate (right axis scale) calculated on the ^{13}CO map by averaging 5° -wide sectors oriented N, S, E and W (continuous and dashed red, and continuous and dashed blue curves, respectively). The magenta line is the average mass-loss rate and the hatched region depicts the typical deviation (see text).

The change of the T_{rot} behaviour around $r = 15''$ does not result from a departure from the ^{12}CO levels from LTE: modelling the $J = 1-0$ and $2-1$ lines and the $^{13}\text{CO}(1-0)$ line with the MADEX statistical equilibrium code (Cernicharo 2012), we find that T_{rot} deviates from T_k by $\lesssim 10\%$ in the range of radii considered here ($0'' \leq r \leq 25''$).

Although the critical densities for the low- J CO transitions ($\approx 1.9 \times 10^3 \text{ cm}^{-3}$ and $1.1 \times 10^4 \text{ cm}^{-3}$, for $J = 1-0$ and $2-1$ lines at ≈ 35 K) are not much lower than the average gas density at $r = 15''$ ($\approx 2.0 \times 10^4 \text{ cm}^{-3}$ – see below), the $^{12}\text{CO}(2-1)$ line opacity ($\tau \approx 4$ for $r = 15''$) prevents a significant departure from thermalization. This is no more the case for the lines of the rare isotope ^{13}CO , which, due to a much lower column density, are out of LTE beyond $\approx 8''$.

Our law of the dependence of T_k on distance r from the star is the first directly derived from very high angular resolution observations. It significantly differs from the lower resolution works of e.g. Doty & Leung (1997) or De Beck et al. (2012), who find beyond $r = 2''$ an exponent q between -1 and -1.2 .

Our exponent -0.68 is significantly shallower than that expected for the adiabatic expansion of a diatomic gas in the vibrational ground state, ≈ -1.2 . This means that the expanding gas is efficiently heated, most likely by dust grains close to the star and by interstellar radiation outside $15''$ (e.g., Huggins et al. 1988).

Indeed, we know that interstellar UV radiation penetrates the envelope as deep as $r = 15''$, since the CCH and CN radicals, which form from the photodissociation of HCCN and HCN (e.g., Millar & Herbst 1994; Glassgold 1996), are first observed near that radius (see Fig. 11). As a matter of fact, a plethora of radicals, such as C_4H , C_3N or MgCCH that are direct or indirect products of photodissociation, are found to peak in abundance at $r = 14-16''$ (Guélin et al. 1993a; Agúndez et al. 2017).

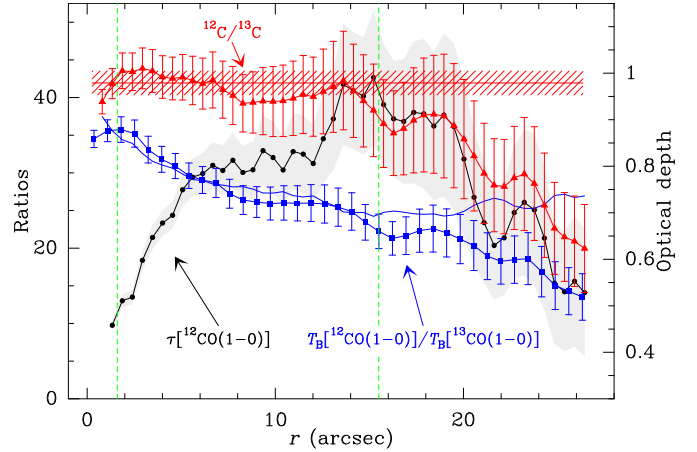


Fig. 22. Ratio of the brightness temperatures of $^{12}\text{CO}(1-0)$ and $^{13}\text{CO}(1-0)$, $^{12}\text{C}/^{13}\text{C}$ isotopic ratio, and optical depth of line $^{12}\text{CO}(1-0)$ against the distance to the star (blue squares, red triangles and black circles, respectively). The continuous blue curve is the brightness temperature ratio calculated with MADEX and the kinetic temperature derived in Sect. 4.3.1. The 1σ uncertainties have been plotted as vertical bars, a grey region, or a hatched rectangle.

Our present observations do not have the angular resolution required to explore the innermost envelope layers ($r \lesssim 1''$). The modelling of high energy lines arising in those layers point to a temperature dependence to r with an exponent $q \approx -0.5$ Fonfría et al. (2008), Agúndez et al. (2012), De Beck et al. (2012), Fonfría et al. (2015). This close to the star, molecules are strongly excited by the radiation from the hot dust cocoon; their collisional deexcitation is a powerful source of heat for the gas that adds up to gas-grain collisions. Further out, the infrared radiation gets diluted and the gas density falls off. We then expect the exponent to steepen from $q \approx -0.5$ to $q = -0.7$ somewhere between $r = 0.5''$ and $1''$.

4.3.2. $^{12}\text{CO}/^{13}\text{CO}$ abundance ratio

In order to directly compare the ^{13}CO and ^{12}CO data, we degraded the spatial resolution of the $^{12}\text{CO}(1-0)$ central velocity-channel maps to $(0.86'' \times 0.76'')$.

From the resulting $^{12}\text{CO}(1-0)$ and $^{13}\text{CO}(1-0)$ line brightnesses and the temperature profile derived in Sect. 4.3.1, we then derived the $J = 1-0$ line opacity τ and the $R_{^{12}\text{C}/^{13}\text{C}} = [^{12}\text{CO}]/[^{13}\text{CO}]$ abundance ratio throughout the meridional plane with the MADEX code. The radial profiles obtained by averaging those quantities in azimuth are displayed in Fig. 22. The isotopic ratio and the mass-loss rate (see Sect. 4.3.3) have been determined at the same time following a self-consistent iterative procedure that can be assumed to converge after ≈ 10 iterations, when the variation between consecutive iterations was $\leq 0.1\%$. We note that, contrary to ^{12}CO , the low J ^{13}CO levels are found to depart significantly from LTE, with a rotation temperature at $r \approx 15''$ to 30% higher than T_k . MADEX indicates that the difference is above 50% beyond $20''$ from the star.

Within the errors, the ratio $R_{^{12}\text{C}/^{13}\text{C}}$ plotted in Fig. 22 appears roughly constant from $r = 1.5''$ to $r = 20''$ (the error bars on the graph only denote the 1σ uncertainty on the line brightnesses). Its value up to the $r = 15''$ shell, 42, agrees well with those determined from the optically thin mm-wave lines of a number of C-bearing molecules (C_4H , HC_3N , SiCC ,...) in that very shell (40–43, see e.g. Cernicharo et al. 2000).

Beyond $20''$, the ratio $R_{12\text{C}/13\text{C}}$ derived with MADEX under the assumption that the ^{12}CO rotation temperature equals T_k , appears to decrease with distance from the star. It seems improbable that the $^{12}\text{C}/^{13}\text{C}$ isotopic ratio has varied in just a few hundred years, because of a dredge-up or of chemical fractionation. Also, selective photodissociation of CO by interstellar UV radiation would increase, not decrease this ratio. Therefore, it is likely that the ^{12}CO levels start to depart from LTE for $r > 20''$, or that the rotation temperature of ^{13}CO is underestimated in our simple model; for example, radiative cascades from higher- J levels pumped by external radiation may overpopulate the $J = 1$ ^{13}CO level. On the other hand, the value of $R_{12\text{C}/13\text{C}}$ found for radii smaller than $20''$ and its near constancy supports our analysis and imply that the derived line opacities and CO column densities are accurate. Assuming the $[\text{CO}]/[\text{H}_2]$ abundance ratio is known, we can then accurately derive the mass loss rate during the last 2000 yr.

4.3.3. Mass-loss rate

The maps in Fig. 20 show evident arcs formed as a consequence of the matter ejection process. The very complex structure noticeable in these maps depicts a set of higher density shells that are expected to be roughly spherically symmetric. Thus, it is possible to estimate the mass-loss rate for every shell along the line-of-sight by using the geometrical information extracted from the map of the optically thin line $^{13}\text{CO}(1-0)$ and its rotational temperature calculated with MADEX from the kinetic temperature derived in Sect. 4.3.1.

The mass-loss rate has been calculated from the brightness temperature averaged over the position angle in four 5° -wide sectors oriented along the N, S, E and W directions (Fig. 21). The mean rate derived after weighting the $r \leq 15''$ data with their uncertainties is $\langle \dot{M} \rangle = (2.7 \pm 0.5) \times 10^{-5} M_\odot \text{ yr}^{-1}$. This value was calculated assuming the ^{12}CO abundance with respect to H_2 of 6×10^{-4} estimated by Agúndez et al. (2012). The estimates beyond $r = 20''$, which seem to show a 30% decrease of the mass loss rate, are not reliable in view of the uncertainties on the large departures to LTE.

The derived average mass-loss rate agrees quite well with most of the values commonly derived or adopted in the literature $\simeq (1.5\text{--}4.0) \times 10^{-5} M_\odot \text{ yr}^{-1}$; see e.g. Keady et al. (1988), Teyssier et al. (2006), Decin et al. (2010), Agúndez et al. (2012), Cernicharo et al. (2015). The mass-loss rate radial profiles for the 5° -wide sectors show variations by factors of up to 3 over scales of a few arcsec (i.e. timescales of $\simeq 10^2$ yr). This reflects the CO column density variation observed between the brightest arcs and the inter-arc region in Fig. 20, typically a factor of 3.

5. Discussion

The ~ 700 yr time delay between the outer arcs corresponds neither to Mira-type oscillations (the IR light period of CW Leo \star is 1.8 yr), nor to the delay between two thermal pulses ($>10^4$ yr for a $2 M_\odot$ TP-AGB star). In previous articles (Guélin et al. 1993a; Cernicharo et al. 2015) we tentatively explained the off-centring of the arcs and their regular spacing by the presence of a companion star on an elliptical orbit in the plane of the sky. The distortion of the Roche lobe during the companion fly-by boosts the mass loss rate at regular intervals close to the binary period. The shells of gas emitted at this stage drift away from the binary system in directions that depends on the system phase at the time of their emission. Numerical simulations – see Fig. 11

of Cernicharo et al. (2015) – show the formation of a pattern of circular arcs fairly similar to that observed with the IRAM 30-m telescope.

The binary star hypothesis may be supported by the detection with the HST of a bright red spot $0.5''$ E of CW Leo \star that Kim et al. (2015) tentatively identify with a companion star. The slight curvature of CW Leo \star 's trajectory between 1995 and 2001, recently reported by Sozetti et al (2017) from an analysis of archival data, may be further evidence for a companion.

Analyzing $^{13}\text{CO}(6-5)$ ALMA observations of a $6''$ -wide field around CW Leo \star , Decin et al. (2015) revisited this hypothesis and argued the inner ^{13}CO position-velocity diagrams are better reproduced by a spiral structure viewed edge-on than by a circular structure viewed face-on. In their model, that stems from Mastrodemos & Morris (1999), the spiral structure results from continuous mass loss in binary star system of period 55 yr, with an orbit viewed edge-on at $\text{PA} \simeq 15^\circ$.

Although the Cernicharo et al. (2015) and Decin et al. (2015) models seem contradictory, they try to explain data relevant to different spatial scales, hence to different epochs. Besides, the Cycle 0 ALMA $^{13}\text{CO}(6-5)$ data, analyzed by Decin et al. (2015), result from a short observing time slot (17 min on-source) and are affected by relatively poor signal-to-noise ratio and uv-plane coverage.

The data presented here have a higher sensitivity and resolution than the previous molecular line studies and a denser uv-plane coverage, allowing us to further investigate the origin of the CO-bright shells. We have seen (e.g. Fig. 11) that the bright ring pattern is strikingly similar for the CO, CN and C_4H lines at radii where all 3 species are present. Given that the CO and C_4H formation paths are quite different and that these species abundances are poorly correlated elsewhere in the envelope, the regions with high line brightness must have large H_2 column densities and the arcs/filaments must trace high mass-loss events. This is corroborated by the excellent positional agreement between the molecular arcs in the meridional plane and the dusty arcs traced by diffused IS light (Fig. 13). The arc/inter-arc contrast is typically 3 for the V-band brightness intensities (Mauron & Huggins 2000) and 2–3 for CO, which, as we have seen, implies gas and dust density contrasts close to 3.

We have shown in Sect. 4 that the bright arcs in the outer envelope are not narrow structures confined to the plane of the sky, but parts of dense spherical shells pertaining to a spherical or near-spherical envelope. The thinness of the shells and their fairly regular spacing set stringent constraints on the mass loss process and the binary star hypothesis. We have repeated the numerical simulations of Cernicharo et al. (2015; based on the periodic ejection near periastron of spherical shells, consisting of free-moving particles, superimposed on a lower intensity continuous mass loss). Within the simple frame of isotropic mass loss, constant expansion velocity and binary orbit orthogonal to the line-of-sight, we found a set of parameters that reproduce the gross features of the observed outer shell pattern Fig. 23).

The $\simeq 16''$ spacing (700 yr time delay) between the brightest outer arcs is found to decrease in the central and youngest part of the envelope (with radius $r < 40''$ and age < 1800 yr – see Fig. 10). It is $10''$ (460 yr) in the NW quadrant between $r = 10''$ and $r = 40''$ ($5''$ in the inner SE quadrant) and only $\simeq 2''$ (90 yr) within $10''$ from CW Leo \star . Are those different patterns generated by a single binary star system and could they denote a rapid change of orbital period during the last 2000 yr? Since CW Leo \star is in a phase of rapid mass loss, let us consider the effect of mass transfer a to the envelope and b to the companion.

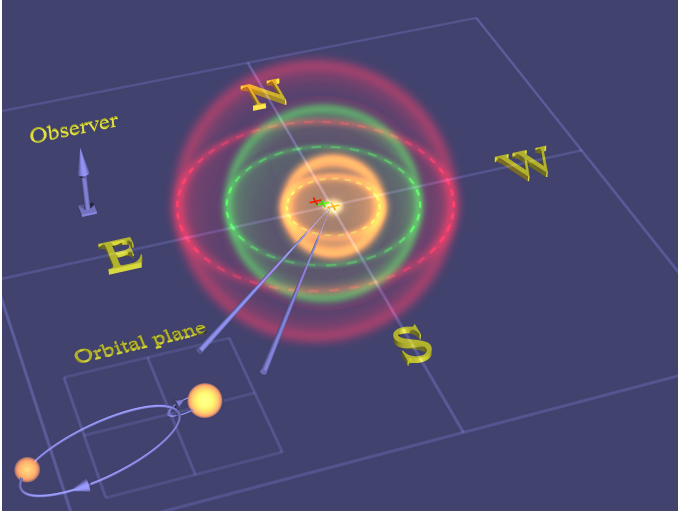


Fig. 23. Schematic view of the 3 brightest shells of the IRC +10216 envelope and (at an enlarged scale) of the binary star system with a mass ratio 4:1 and eccentricity 0.92, orbiting in the plane of the sky. The figure was generated with the POV-Raytracer 3.6.1 software (Persistence of Vision Pty. Ltd., Williamstown, Victoria, Australia, <http://www.povray.org/>).

- a) The isotropic ejection by CW Leo★ of an amount of matter $-dM$ into the envelope, i.e. beyond the binary orbit, reduces the binary system mass $M = M_1 + M_2$ and tends to *increase* the system orbital period (from T to $T' = T [M/(M - dM)]^{3/2}$). However, the present rate of mass loss to the envelope ($\dot{M}_1 = 2.7 \times 10^{-5} M_\odot \text{ yr}^{-1}$) is too small to noticeably affect the period over just a few thousand years.
- b) A mass transfer dM from CW Leo★ to a *less massive* companion ($M_2 < M_1$), on the other hand, would *decrease* the orbital period (to first approximation from T to $T' = T (M_1 M_2 / [(M_1 - dM)(M_2 + dM)]^3)$, hence increase the frequency of fly-bys, the sought effect.

The present mass of CW Leo★ may be estimated in the range $0.6\text{--}1.2 M_\odot$. This stems from its main sequence mass $1.6 M_\odot$ derived from the envelope isotopic composition (Guélin et al. 1995; De Nutte et al. 2017), and from different evaluations of the envelope mass – between $0.3 M_\odot$, the gas mass expelled during the last 10^4 yr (Cernicharo et al. 2015), and $1 M_\odot$, the mass expelled since the formation of the astrosphere, 7×10^4 yr ago (Sahai & Chronopoulos 2010). The $1 M_\odot$ figure assumes the mass loss rate linearly increased by a factor of 10 during that time interval – see Fig. 19 of Steffen et al. (1998).

Assuming the mass of CW Leo★ is $M_1 = 1 M_\odot$ and that of its companion is $M_2 = 0.2 M_\odot$ (red dwarf of class M4V), the transfer of $0.1 M_\odot$ from CW Leo★ to the companion would shorten the orbital period by almost a factor of 2. However, the transfer of $dM = 0.1 M_\odot$ during the last 2000 yr would imply a rate of mass transfer to the red dwarf twice larger than to the envelope.

The companion cannot be very massive and the mass transfer should have started only recently, since we see in the outer envelope no traces of direct gravitational interaction with the companion. The shape of binary star envelopes has been investigated by Kim & Taam (2012), Kim et al. (2017) for various expansion velocities, stellar masses and orbit sizes and ellipticities. A near-spherical symmetry implies the outer envelope was predominantly shaped by an isotropic wind at V_{exp} and, to a lesser degree, by the orbital motion of the mass-losing star (V_o , the so-called

reflex motion). A third envelope shaping mechanism, the tidal wake generated by the companion’s motion, should have created a flattened oblate structure, which is not observed. This means that $V_{\text{exp}} \gg V_o$, $M_2 < M_1$ and/or that the distance between the stars is large, which is consistent with our finding that $V_{\text{exp}} = 14.5 \text{ km s}^{-1}$, $V_o \approx 2 \text{ km s}^{-1}$ according to the observed outer arc offsets, and $T \approx 700 \text{ yr}$.

In summary, a possible scenario that explains both the outer and inner envelope morphologies, is then that the shells are ejected during a short period of interaction between CW Leo★ and a low-mass companion on a long period eccentric orbit. According to Moeckel & Bate (2010), Kouwenhoven et al. (2010) and references therein, binary systems of large separation can form during the dissolution phase of an open cluster, due to late captures. About 15% of the binaries belong to this group, a fairly large probability. Although, it was thought that such eccentric systems would necessarily evolve toward stable circular orbits, the observation of eccentric companions in planetary nebulae (PNe) shows that such systems may remain as such for a very long time (Jones & Boffin 2017a).

The companion on an eccentric orbit may come very close to CW Leo★ and strongly interact with it. Near periastron, CW Leo★’s extended atmosphere (its photosphere radius is 2.5 AU Fonfría et al. 2015) may exceed the Roche limit, which shrinks as the companion comes closer. This would raise a near-spherical shell of gas up to the dust condensation radius (to be later accelerated by radiation pressure and expelled into the envelope) and, in parallel, cause a burst of mass transfer to the companion. In an evolved phase that may have started a few thousand years ago, the companion may even pass through the upper atmosphere of the AGB star, accrete mass and experience drag, while resisting evaporation if its mass is sufficient – e.g. $>10^{-2} M_\odot$ Soker et al. (1998). The densification of the bright shells observed between the outer and the inner envelope, and the apparent increase in the frequency of dense shell ejections, would then be due to a gradual reduction in eccentricity and orbital period of the companion.

Another way to explain the change in spacing between the outer and inner ejected shells, would be to speculate that the orbit eccentricity is small and that the star separation remains near its minimum during a fair fraction of the period. This may give rise to multiple short-duration mass loss episodes in the course of a single fly-by. The thin shells expelled during such events expand quickly, while keeping the momentum induced by CW Leo★’s orbital motion, and drift away from the binary in different directions. The spacing and centring of the shells in a time scale of few hundred years would then be irregular, an effect that smears off at later times.

Alternately, we may consider that the outer shell pattern is regulated by shocks in the expanding gas. The expansion velocity is much higher than the sound velocity in the envelope, hence is prone to create shocks when the gas velocity is not quite uniform, or if the gas cannot freely escape into outer space. This is the case, in particular, when the gas velocity in the envelope is modulated by the orbital motion of a binary system. The simulations of Kim & Taam (2012) of a continuous isotropic outflow of large velocity (their model M6) show that dense shells are created where the outflowing gas, accelerated by the star orbital motion, catches up to the gas expelled when the star was moving in the opposite direction. The difference in velocities, $2V_o$, is larger than the sound velocity $\approx 0.4 \text{ km s}^{-1}$, so that a strong shock occurs. The density increases (and the velocity differential decreases) from upstream to downstream of the shock – the

predicted increase (decrease) is a factor of ≈ 4 at large radii, similar to the observed gas density contrast (see Sect. 4.3.3).

We have searched for signatures of shocks in the velocity field near the arcs. From the CO, CN and C₄H PV diagrams (e.g. Fig. 17) we see no traces of a 2 km s⁻¹ spread in the line-of-sight velocity component, but, of course, have no kinematical information for the perpendicular directions. If the eccentricity of the shells is caused by a binary star system, the orbital plane should be almost perpendicular to the line-of-sight.

Finally, a third possibility would be that the star system is not binary, but triple, allowing multiple periods and different interaction configurations. Whereas triple stars are common in early stellar phases, the two closest stars tend with time to form a common-envelope and to merge. Yet, [Soker \(2016\)](#) argue that triple star systems may survive up to the AGB stage: from the images of hundreds of PNe they find that one in six seems to host such a system. However, as pointed up by [Jones & Boffin \(2017b\)](#), so far only one PN has been actually demonstrated to host 3 stars at its center, on the basis of velocity variations.

6. Summary and conclusion

The main findings of our IRC +10 216 observations can be summarized as follows:

- 1) The star CW Leo★ and its hot dust cocoon appear in the 1.2 mm continuum as a 0.33 Jy Gaussian source of diameter 0.21''.
- 2) In the CO(2–1) line, the envelope consists of a strong, fairly compact source, centred on the star, plus a slowly decreasing component, extending up to $r = 3'$ from CW Leo★ and a series of bright shells that modulate the extended component.
- 3) Outside the dust acceleration region, the envelope expands radially at a remarkably constant velocity, 14.5 km s⁻¹, with a small turbulent velocity (≤ 0.6 km s⁻¹).
- 4) At the star velocity, i.e. in the plane of the sky passing through the star, the bright shells trace a pattern of circular arcs as thin as the 3'' SMA beam. Outside radius $r = 40''$, the brightest arcs are nearly concentric and regularly spaced, with an average separation of 16'', or 700 yr in expansion time. They are centred a few arcsec on either side of CW Leo★.
- 5) Inside radius $r = 40''$, ALMA reveals a denser, less regular arc pattern. The typical separation between the brightest arcs decreases, a change that can hardly be attributed to the ten-fold higher resolution, since smoothed to 3'', the ALMA arcs follow the SMA inner arcs. ALMA resolves the bright arcs into thin circular filaments off-centred from CW Leo★ by a fraction of an arcsec for the smallest arcs, up to a couple of arcsec for the largest (20–30''). Some filaments west of the star appear kinked.
- 6) The pattern of bright CO arcs is accurately replicated in the CN and C₄H line emissions, wherever these radicals are present, as well as in the dust structures traced by scattered light. They must trace gas shells ≈ 3 times denser than the intershell regions.
- 7) The gas kinetic temperature in the central region follows from $r = 0.5''$ to $r = 15''$ the power law $T_{\text{rot}} = (256.9 \pm 1.5)(r/0.8)^{-(0.675 \pm 0.003)}$ K, and settles around 35 K until at least $r = 25''$. The mass loss rate during the last 10³ yr was $\langle \dot{M} \rangle = (2.7 \pm 0.5) \times 10^{-5} M_{\odot} \text{ yr}^{-1}$ on the average, with peak-to-peak variations of a factor of 3. The ¹²CO/¹³CO abundance ratio is found equal to 42 in the central region.
- 8) A 3D reconstruction of the outer envelope shows the dense shells have nearly spherical shapes, extending typically over one or more steradians. The envelope shows little or no signs of flatness.

The outer envelope structure (the spherical shape of the shells and their small eccentricity) may be explained by continuous mass loss plus short mass-loss episodes triggered by the fly-by of a companion star with a 700 yr period and orbit nearly perpendicular to the line-of-sight. The orbital velocity of the AGB star is typically 1–2 km s⁻¹ during the episodes of high mass loss.

The structure observed in the central region of the envelope, where the shells are denser, less regular and show no obvious signature of a spiral, is more difficult to explain. It may have been shaped by the companion star described above, if its mass is much lower (e.g. 1/5th) than the mass the AGB star, and if a large transfer of mass to the companion has developed during the last 2000 yr. Alternately, the central system may consist of more than two massive bodies.

Long term very high angular resolution monitoring of the compact central source in the visible, IR or the sub-mm continuum may allow us to further investigate its nature. The dim source spotted by [Kim et al. \(2015\)](#) on HST images, and the slight curvature of the CW Leo★ track on the sky could be first evidence for a multiple system.

Acknowledgements. We thank S. Guilloteau and S. Bardeau for their help on the GILDAS software and J. M. Winters for helpful comments. This paper makes use of data from the following instruments: The Submillimeter Array (SMA project number 2011B-S052, 2012B-S004, and 2012B-S101), IRAM single dish telescope and interferometer (projects t020, v018), ALMA (ADS/JAO.ALMA#2013.1.01215.S). The work was partly supported by the CNRS program ‘‘Physique et Chimie du Milieu Interstellaire’’ (PCMI). M.G. also acknowledges support for travel by the SMA. We thank Spanish MICINN for funding support through grants AYA2006-14876, AYA2009-07304 and the CONSOLIDER program ‘‘ASTROMOL’’ CSD2009-00038, and the European Research Council for funding support through the European Union’s Seventh Framework Program (FP/2007-2013)/ ERC Grant Agreement No. 610256 NANOCOSMOS.

References

- Agúndez, M., Fonfría, J. P., Cernicharo, J., et al. 2012, *A&A*, **543**, A48
 Agúndez, M., Cernicharo, J., Quintana-Lacaci, G., et al. 2017, *A&A*, **601**, A4
 Becklin, E. E., Frogel, J. A., Hyland, A. R., Kristian, J., & Neugebauer, G. 1969, *ApJ*, **158**, L133
 Bremer, M. 1995, *A&AS*, **112**, 551
 Cernicharo, J. 2012, in *EAS Pub. Ser.* 58, eds. C. Stehlé, C. Joblin, & L. d’Hendecourt, 251
 Cernicharo, J., Guélin, M., & Kahane, C. 2000, *A&AS*, **142**, 181
 Cernicharo, J., Daniel, F., Castro-Carrizo, A., et al. 2013, *ApJ*, **778**, L25
 Cernicharo, J., Marcelino, N., Agúndez, M., & Guélin, M. 2015, *A&A*, **575**, A91
 Cordiner, M. A., & Millar, T. J. 2009, *ApJ*, **697**, 68
 De Beck, E., Lombaert, R., Agúndez, M., et al. 2012, *A&A*, **539**, A108
 De Nutte, R., Decin, L., Olofsson, H., et al. 2017, *A&A*, **600**, A71
 Decin, L., Agúndez, M., Barlow, M. J., et al. 2010, *Nature*, **467**, 64
 Decin, L., Royer, P., Cox, N. L. J., et al. 2011, *A&A*, **534**, A1
 Decin, L., Richards, A. M. S., Neufeld, D., et al. 2015, *A&A*, **574**, A5
 Doty, S. D., & Leung, C. M. 1997, *MNRAS*, **286**, 1003
 Fonfría, J. P., Cernicharo, J., Richter, M. J., & Lacy, J. H. 2008, *ApJ*, **673**, 445
 Fonfría, J. P., Cernicharo, J., Richter, M. J., et al. 2015, *MNRAS*, **453**, 439
 Fonfría, J. P., Hinkle, K. H., Cernicharo, J., et al. 2017, *ApJ*, **835**, 196
 Gerhard, O. E., & Binney, J. J. 1996, *MNRAS*, **279**, 993
 Glassgold, A. E. 1996, *ARA&A*, **34**, 241
 Groenewegen, M. A. T., van der Veen, W. E. C. J., Lefloch, B., & Omont, A. 1997, *A&A*, **322**, L21
 Guélin, M., Lucas, R., & Cernicharo, J. 1993a, *A&A*, **280**, L19
 Guélin, M., Zylka, R., Mezger, P. G., et al. 1993b, *A&A*, **279**, L37
 Guélin, M., Forestini, M., Valiron, P., et al. 1995, *A&A*, **297**, 183
 Hubert, B., Opitom, C., Hutsemékers, D., et al. 2016, *Icarus*, **277**, 237
 Huggins, P. J., Olofsson, H., & Johansson, L. E. B. 1988, *ApJ*, **332**, 1009

- Jones, D., & Boffin, H. M. J. 2017a, [Nat. Astron.](#), **1**, 0117
- Jones, D., & Boffin, H. M. J. 2017b, [MNRAS](#), **466**, 2034
- Kaastra, J. S. 1989, [A&A](#), **224**, 338
- Keady, J. J., Hall, D. N. B., & Ridgway, S. T. 1988, [ApJ](#), **326**, 832
- Kim, H., & Taam, R. E. 2012, [ApJ](#), **759**, 59
- Kim, H., Lee, H.-G., Maun, N., & Chu, Y.-H. 2015, [ApJ](#), **804**, L10
- Kim, H., Trejo, A., Liu, S.-Y., et al. 2017, [Nat. Astron.](#), **1**, 0060
- Kouwenhoven, M. B. N., Goodwin, S. P., Parker, R. J., et al. 2010, [MNRAS](#), **404**, 1835
- Leão, I. C., de Laverny, P., Mékarnia, D., de Medeiros, J. R., & Vandame, B. 2006, [A&A](#), **455**, 187
- Lucas, R., & Guélin, M. 1999, in *Asymptotic Giant Branch Stars*, eds. T. Le Bertre, A. Lebre, & C. Waelkens, IAU Symp., 191, 305
- Mastrodemos, N., & Morris, M. 1999, [ApJ](#), **523**, 357
- Mauron, N., & Huggins, P. J. 2000, [A&A](#), **359**, 707
- Mauron, N., & Huggins, P. J. 2006, [A&A](#), **452**, 257
- Menten, K. M., Reid, M. J., Krügel, E., Claussen, M. J., & Sahai, R. 2006, [A&A](#), **453**, 301
- Menten, K. M., Reid, M. J., Kamiński, T., & Claussen, M. J. 2012, [A&A](#), **543**, A73
- Millar, T. J., & Herbst, E. 1994, [A&A](#), **288**, 561
- Moeckel, N., & Bate, M. R. 2010, [MNRAS](#), **404**, 721
- Neugebauer, G., & Leighton, R. B. 1969, NASA Spec. Publ., 3047
- Palmer, P. L. 1994, [MNRAS](#), **266**, 697
- Quintana-Lacaci, G., Cernicharo, J., Agúndez, M., et al. 2016, [ApJ](#), **818**, 192
- Ramstedt, S., Schöier, F. L., Olofsson, H., & Lundgren, A. A. 2008, [A&A](#), **487**, 645
- Rybicki, G. B. 1987, in *Structure and Dynamics of Elliptical Galaxies*, ed. P. T. de Zeeuw, IAU Symp., 127, 397
- Sahai, R., & Chronopoulos, C. K. 2010, [ApJ](#), **711**, L53
- Sault, R. J., Teuben, P. J., & Wright, M. C. H. 1995, in *Astronomical Data Analysis Software and Systems IV*, eds. R. A. Shaw, H. E. Payne, & J. J. E. Hayes, ASP Conf. Ser., 77, 433
- Soker, N. 2016, [MNRAS](#), **455**, 1584
- Soker, N., Rappaport, S., & Harpaz, A. 1998, [ApJ](#), **496**, 842
- Steffen, M., Szczerba, R., & Schoenberner, D. 1998, [A&A](#), **337**, 149
- Teyssier, D., Hernandez, R., Bujarrabal, V., Yoshida, H., & Phillips, T. G. 2006, [A&A](#), **450**, 167
- Von Zeipel, H. 1908, [Annales de l'Observatoire de Paris](#), **25**, F.1

Appendix A: Spherical deprojection of the X, Y, V CO datacubes

A number of techniques have been elaborated to take account of the projection effects that are a daily problem in astronomy. Other than model fitting, deprojection recovers a spatial emissivity structure based on ad hoc symmetry assumptions. Compared to a typical model fit, it allows the recovery of more detailed structures at the cost of purely geometrical rather than physical constraints; it is well adapted to objects that by nature exhibit a prominent symmetry.

Spherical deprojections based on the Abel transform were used by Von Zeipel (1908) on globular clusters. Kaastra (1989) extended the method to cylindrical symmetry for a reconstruction of *Tycho's* supernova remnant. Hubert et al. (2016) combined the Abel transform with least-squares fits to triangular profiles to reconstruct cometary atmospheres. However, going further than spherical symmetry makes the results ambiguous.

The principal difference between deprojection and a tomographic 3D reconstruction resides in the uniqueness of the observer's viewing angle for deprojection, uniqueness that may lead to fallacious representations. Rybicki (1987) argued that the Fourier slice theorem made it impossible to recover information from inside a “cone of ignorance” of half-opening angle θ for an object whose symmetry axis is tilted by θ relative to the plane of the sky; Palmer (1994) constructed a Legendre-polynomial based expansion for density distributions that met the condition that each single term must not be based exclusively on terms within the cone of ignorance, requiring an absence of abrupt changes in the density distribution. An iterative deprojection algorithm was presented by Bremer (1995), but although the method was stable enough to support noisy images and deconvolution it found its limits at the cone of ignorance. Gerhard & Binney (1996) demonstrate how axisymmetric density distributions can be constructed that are invisible when observed under a range of inclination angles; such distributions may be added and subtracted arbitrarily from a deprojected cylindrical density distribution without changing the projection. The infinite variety of those functions showed that the absence of abrupt density changes was not enough to call a distribution sufficiently “well behaved” to justify its deprojection. Only when the symmetry axis is in the plane of the sky is the cylindrical symmetry deprojection unique.

For our deprojection analysis of the IRC +10 216, we place the symmetry constraints on the velocity field, assuming a constant spherical expansion velocity. As seen in Sect. 4.1, this assumption is justified by the shape of the bright arcs in the position-velocity diagrams and the similarity of the line widths for the various tracer molecules of the envelope, both of which point to a constant expansion velocity of 14.5 km s^{-1} .

From the position-velocity datacube (spatially resolved in x and y and binned in the line of sight velocity component, V , with steps of $\Delta V = 1 \text{ km s}^{-1}$) we first generate a set of velocity-channel maps, each corresponding to the integral along the line of sight of the signals emitted within its velocity bin. We note that for a spherical volume and a uniform expansion velocity, V_{exp} , the 1 km s^{-1} -wide bins define spherical sectors of equal volume (see Fig. A.1). Close to the line of sight towards the observer, we have to expect a final cone of half-opening angle $\alpha = \arccos(1-2/nc) \simeq 21^\circ$, where $nc = 2V_{\text{exp}}/\Delta V$ is the number of spectral channels required to sample the sphere.

Starting from the (x, y, V) datacube, we follow two different approaches for the reconstruction of the spatial 3D envelope morphology. Both assume a constant expansion velocity,

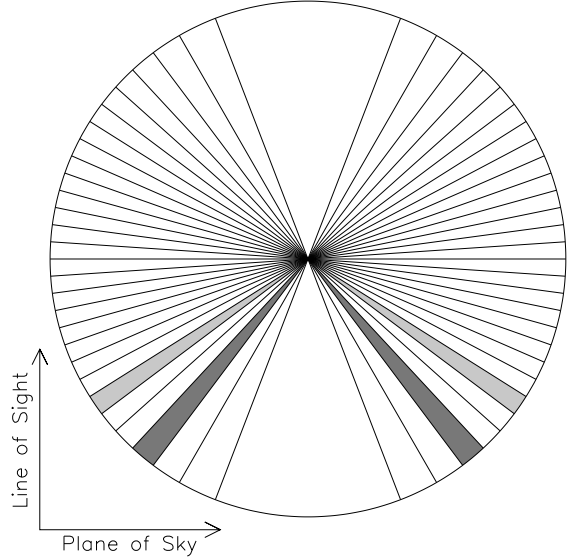


Fig. A.1. Volumes sampled in the velocity image of a sphere expanding at constant velocity. A total of $nc = 30$ velocity channels was assumed here; light and dark grey represent volumes projected into the fourth and seventh channel, respectively.

discarding additional motions in the plane of the sky that are unobservable. Both also assume that the observed CO signals are proportional to the gas column density.

- A: *Non-iterative code*. The code works with Cartesian coordinates. It starts from the central velocity-channel map ($V = V_*$ bin) and moves alternately towards the adjacent external velocity bins. For every pixel x, y in the sky plane, it identifies from the pre-defined velocity field the coordinate range along the line of sight (z direction) that corresponds to each velocity bin. For the first bin ($V = V_* \pm \Delta V/2$), it evenly distributes the emission observed toward each x, y pixel over all cells in the allowed z segment. Turning to the next velocity bin, it first sets the emissivity in each x, y, z cell of that velocity range by taking the average value of its closest known neighbours. Then, it calculates for every x, y the integral of this first guess over z and compares it to the observed signal in the velocity-channel map. The difference guessed-observed, weighted by the square of the distance to the closest neighbours, is subtracted from the guessed values, starting from the most distant (highest weight) cell to the closest cell; if the subtraction yields a negative value, the latter is set to zero and the value to be subtracted carried over to the next z cell. The main time consuming feature of this code is the distance weighting and the sorting.
- B: *Iterative code*. This code switches back and forth from Cartesian to spherical coordinates. It first *uniformly* spreads the emissivity observed in every velocity-channel map for each x, y pixel over all z cells allowed for that bin. Next, it resamples by linear interpolation the so derived emission model onto a spherical coordinate grid (r, ϕ, θ) . Then it performs in spherical coordinates a series of smoothing steps along the polar (θ) angle with a weighting that tends to diffuse the signal toward the polar regions. Finally, it interpolates back the emission into the Cartesian 3D grid, calculates the resulting velocity-channel image and normalizes the result to match the input image. The interpolation/diffusion steps are repeated until a stable solution is obtained.

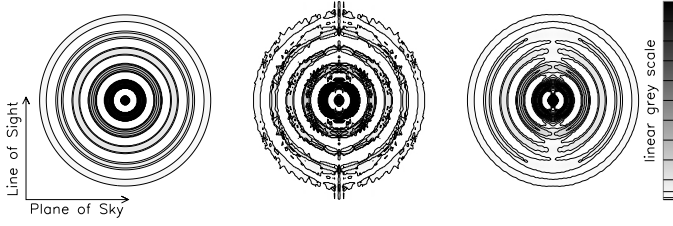


Fig. A.2. Case (1). Concentric shells of diminishing emissivity, *from left to right*: Synthetic distribution, reconstruction with method A and finally B. Intensity scales are identical for all three.

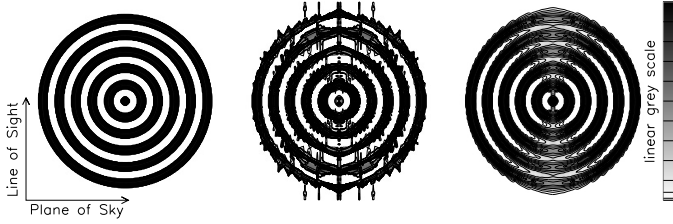


Fig. A.3. Case (2). Concentric shells of constant emissivity, *from left to right*: Synthetic distribution, reconstruction with method A and finally B. Intensity scales are identical for all three.

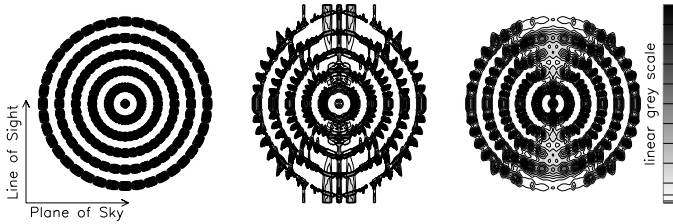


Fig. A.4. Case (3). Concentric shells of constant emissivity with a strong modulation in the spherical θ direction, *from left to right*: Synthetic distribution, reconstruction with method A and finally B. Intensity scales are identical for all three.

The density reconstruction algorithms run into three problems, all the more severe when close to the incoming/receding polar caps:

- *Line opacity*: The $^{12}\text{CO}(2-1)$ line opacity in IRC +10 216 is fairly large. It is typically 1–2 in the central velocity-channel and reaches values up to 3–4 between $r = 10''$ and $20''$ (see Sect. 4.3.2). In the outer ($r > 40''$) envelope, however, the

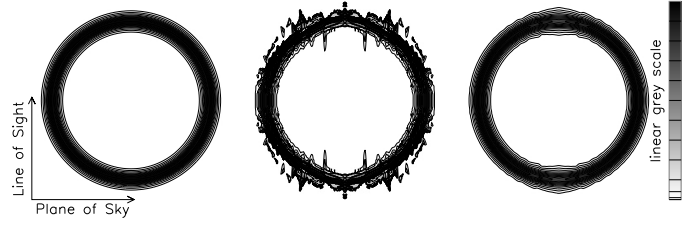


Fig. A.5. Case (4). A simple expanding shell, *from left to right*: Synthetic distribution, reconstruction with method A and finally B. Intensity scales are identical for all three.

line become subthermally excited, so its intensity roughly remains proportional to the CO column density, validating our above approach. Such is not the case, however, near the extreme velocities, where the line opacity becomes much larger.

- *Degeneracy*: velocity degeneracy does not allow to fully reconstruct the emission along the lines of sight crossing the cone-shaped regions with the most extreme velocities. The algorithms only do an extrapolation, which is tested for consistency against the velocity image.
- *Gridding*: the innermost part of the envelope is the brightest part in $^{12}\text{CO}(2-1)$. Its small-scale structure would require a denser gridding in the calculation of the velocity image.

This explains why the 3D reconstructions of the CO envelope have difficulties closing the dense shells near the poles. The position-velocity diagrams of other molecular gas tracers, e.g. the optically thin C_4H lines, strongly suggest that the shells do close near the line of sight to the observer. We can trace the shells over large angular ranges of about 90 degrees outside the plane of the sky (see e.g. Fig. 19) and about 120 degrees inside (Fig. 10). The morphology is rich in narrow spurs bridging the shells, which may indicate remnants of shells emitted at slightly different phases in the orbit. The degree of interaction between the shells is not strong enough to produce a telltale broadening of the observed spectral lines.

Both methods have their advantages and drawbacks, which we demonstrate with four numerical testcases in Figs. A.2–A.5 that were calculated under conditions matching the observations for IRC +10 216. Code A allows a better conservation of the contrast between different shells at the price of a higher noise level in the reconstructed cube, while code B produces smoother distributions with a loss in contrast at θ angles close to the poles.